AEDODYNAMIC DESIGN OF THE SPACE SHUTTLE ORBITER

by

W.E. Bornemann
Manager, Space Shuttle Aerodynamics
Rockwell International Corporation
Space Systems Group
12214 Lakewood Boulevard
Downey, CA 90241

and

T.E. Surber
Supervisor, Orbiter Aerodyanmics
Rockwell International Corporation
Space Systems Group
12214 Lakewood Boulevard
Downey, CA 90241

SUMMARY

The Space Shuttle Vehicle is being developed by the NASA to provide capability for lower cost space operations in the 1980's and beyond. This paper describes Shuttle Orbiter aerodynamic design conducted by Rockwell International under contract to NASA. Aerodynamic criteria key to establishing the external configuration are discussed together with evolution of the design including effects of wing-body blending on high angle of attack aerodynamics.

An overview of the wind tunnel program is given and aerodynamic characteristics of the final configuration are described. Aerodynamic parameters critical to definition of Orbiter entry control and performance are identified. During entry, the Orbiter flies over an angle of attack range from 50 to zero degrees. Trim capability and stability and control characteristics are discussed at critical regions in the entry trajectory. Methods are described to define reaction control rocket effectiveness and aerodynamic interactions during the initial portion of entry. At hypersonic speeds, wind tunnel results of viscous interaction effects at high angles of attack are discussed. In the supersonic region where transition from high to low angle of attack occurs, critical stability and control parameters and wind tunnel results are described. At subsonic speeds, comparisons are shown between predicted aerodynamic characteristics and data from the approach and landing flight test program.

NOMENCLATURE

Acronyms

AEDC	Arnold Engineering Development Center
ALT	Approach and Landing Test
ARC	NASA Ames Research Center
ATP	Authority to Proceed
CDR	Critical Design Review
EAFB	Edwards Air Force Base
ET	External Tank
ETR	Eastern Test Range
FCF	First Captive Flight
FMOF	First Manned Orbital Flight
JSC	NASA Johnson Space Center
KSC	NASA Kennedy Space Center
LaRC	NASA Langley Research Center (also LRC)
OMS	Orbital Maneuvering System
OV	Orbital Vehicle
PDR	Preliminary Design Review
PRR	Program Requirements Review
RCS	Reaction Control System
SRB	Solid Rocket Booster
SSME	Space Shuttle Main Engine
TAEM	Terminal Area Energy Management
WTR	Western Test Range

Symbols

b	Span
C_A	Axial force coefficient
C_D	Drag force coefficient
C_L	Lift coefficient
C_ℓ	Rolling moment coefficient
C_{ℓ_β}	Rolling moment coefficient due to sideslip (per degree)
$C_{\ell_{\delta a}}$	Rolling moment coefficient per degree aileron deflection
$C_{\ell_{\delta r}}$	Rolling moment coefficient per degree rudder deflection
C_m	Pitching moment coefficient
C_N	Normal force coefficient
C_n	Yawing moment coefficient
C_{n_β}	Yawing moment coefficient due to sideslip
$C_{n_{\delta a}}$	Yawing moment coefficient per degree aileron deflection
$C_{n_{\delta r}}$	Yawing moment coefficient per degree rudder deflection
C'_∞	Factor of proportionality in linear viscosity-temperature relation, equation (5)
CG	Center of gravity
h	Altitude
L/D	Lift-to-drag ratio
M	Mach number
M.A.C.	Mean aerodynamic chord, also $\bar{c}$
$\frac{m_j}{m_\infty}$	RCS jet mass flow ratio, equation (4)
$\bar{q}$	Dynamic pressure = $1/2\rho V^2$
RE	Reynolds number, also R_e
S	Reference area
S_e	Standard error of estimate
V_D	Design touchdown speed
$\bar{V}'_\infty$	Viscous parameter, equation (2)
$\bar{x}_\infty$	Viscous interaction parameter, equation (1)
α	Angle of attack
β	Angle of sideslip (positive nose-up)
δ_a	aileron deflection (positive for positive rolling moment)
δ_{BF}	Body flap deflection (positive for nose-down pitching moment)
δ_e	Elevator deflection (positive for nose-left yawing moment)
σ	Standard deviation
$\frac{\phi_j}{\phi_\infty}$	RCS jet momentum ratio, equation (3)
Λ	Sweep angle
λ	Taper ratio
ρ	Mass density of air

Subscripts

LB	Body length
∞	Freestream

INTRODUCTION

The Space Shuttle Vehicle is being developed by the NASA to provide capability for lower cost space operations in the 1980's and beyond. The flight vehicle consists of a reusable orbiter, an expendable external propellant tank, and two reusable solid rocket boosters. Space Shuttle will be capable of launching a variety of payloads into earth-orbit from either the Eastern Test Range (ETR) at Kennedy Space Center or the Western Test Range (WTR) at Vandenberg Air Force Base. Maximum payload capabilities will be 29,480 kg for an easterly launch from ETR and 14,515 kg for launch into polar orbit from WTR.

The orbiter development contract, under the direction of NASA's Johnson Space Center, was awarded to Rockwell International in August 1972. Under this contract, two orbiter vehicles are being built-OV101 was delivered to the flight test center in February 1977, and approach and landing flight testing completed in October 1977. OV102, the first orbital flight vehicle, is in assembly and is scheduled for roll-out in late 1978. Orbital flight testing will begin in 1979.

Aerodynamic considerations have played a significant role in the vehicle design process. The Shuttle must fly satisfactorily with predicted aerodynamic characteristics; it is not feasible to approach flight testing by incremental expansion of the altitude and velocity envelope. Consequently, the NASA and Rockwell have given careful attention to the development of an extensive data base derived largely from wind tunnel tests, with detailed attention being given to defining uncertainties through statistical analysis of wind tunnel data and by comparisons of wind tunnel predictions with flight data from previous programs. In addition, the flight control system is being designed to minimize its sensitivity to uncertainties in aerodynamic parameters.

The objectives of this paper are to: (1) briefly describe the Shuttle mission in order to identify key aerodynamic design criteria; (2) summarize aerodynamic development of the orbiter; (3) describe the key aerodynamic parameters and their relationship to design and performance of the entry flight system; and (4) summarize recent flight results which verify the aerodynamic estimates for the approach and landing phase of the Shuttle mission.

VEHICLE/MISSION DESCRIPTION

The Shuttle Vehicle consists of four major elements: the orbiter; main engines (SSME); external tank (ET); and two solid rocket boosters (SRB). Overall vehicle configuration is illustrated in Figure 1. The external tank contains the liquid oxygen/liquid hydrogen propellants used by the main engines during ascent. Liquid oxygen is located in the forward tank to maintain an acceptable center of gravity for the combined vehicle. Nozzles on each booster are gimballed to augment control during ascent.

The orbiter, Figure 2, is a double-delta wing configuration comparable in size to a modern transport aircraft. Normally, the orbiter carries a crew of four—commander, pilot, mission specialist, and payload specialist—with provision for as many as seven persons. The orbiter can remain in orbit nominally for seven days (up to 30 with special payloads), return to earth with personnel and payload, land like an airplane, and be refurbished for a subsequent flight in 14 days. Three main rocket engines mounted in the aft section of the orbiter provide propulsive thrust during ascent. These two million Newton thrust liquid oxygen/liquid hydrogen engines are gimballed in pitch and yaw to provide thrust vector control. Smaller orbital maneuvering system (OMS) rocket engines are also located in the aft section to provide final impulse for orbit insertion, orbital maneuvers, and deorbit. Reaction control rockets (RCS) are located in both the forward and aft section of the orbiter to provide attitude control and three-axis translation during orbit insertion and on-orbit operations. The aft reaction control rockets are used in combination with aerodynamic surfaces for control during entry. Aerodynamic surface controls include split elevons along the wing trailing edge; a split rudder in the vertical fin which can also be flared open to serve as a speed brake during descent; and a hinged body flap located at the lower aft end of the fuselage to augment control during descent and landing approach. The body flap also shields the exposed main engine nozzles from aerodynamic heating during entry.

The entire external surface of the orbiter, except the windows, is protected by reusable insulation to maintain acceptable structural temperatures under entry heating environment. Figure 3 illustrates the application areas for the materials used in the thermal protection subsystem. Application is as follows:

1. Coated Nomex felt is used in areas where temperatures are less than 672°K for entry and 716°K for ascent; i.e., upper cargo bay door, mid- and aft-fuselage sides, upper wing, and OMS pod.

2. Low-temperature reusable surface insulation is used in those areas where temperatures are below 922°K and above 672°K under design heating conditions.

3. High-temperature reusable surface insulation is used in those areas exposed to temperatures below 1533°K and above 922°K under design heating conditions.

4. Reinforced carbon-carbon is used on areas such as wing leading edge and nose cap where predicted temperatures exceed 1533°K under design heating conditions.

5. Thermal window panes are used in the crew compartment and high temperature metal is used for forward reaction control system fairings and elevon upper surface rub seal panels.

6. Thermal barriers are installed around operable penetrations (main egress hatch, landing gear doors, etc.) to protect against aerothermal heating.

The thermal protection system is a passive system. It has been designed for ease of maintenance and for flexibility of ground and flight operations while satisfying its primary function of maintaining acceptable airframe outer skin temperatures.

Mission Profile

Mission performance capability is summarized in Table 1. A typical mission profile is shown in Figure 4. The Shuttle is launched with the main engines and solid rocket boosters burning in parallel. A maximum dynamic pressure of 31,100 N/m^2 is experienced approximately 62 seconds after launch at 11,280 meters altitude. Booster separation occurs at 122 seconds at an altitude of 43,280 meters, 46.3 kilometers downrange from the launch site. The solid rocket boosters descend on parachutes, are recovered after water impact, and are refurbished for subsequent reuse.

After booster separation, the orbiter continues to ascend with main engine cut-off and external tank separation occurring 479 seconds after lift-off when the orbiter has reached an altitude of 115,700 meters. The orbital maneuvering system engines, which provide the additional velocity needed for orbital insertion are cut-off approximately 600 seconds after launch.

After completion of the orbital operations phase, deorbit is accomplished by retro-fire of the orbital maneuvering engines, and the orbiter descends to the atmospheric entry interface (nominally, an altitude of 121,920 meters). A typical entry trajectory is shown in Figure 5. The initial entry phase extends to a dynamic pressure level of 957.6 N/m^2 (approximately 76,200 meters altitude) during which attitude control from two aft pods is blended with aerodynamic surface controls, the latter gaining in effectiveness as dynamic pressure increases. Entry, from a dynamic pressure level of 957.6 N/m^2 to a Mach number of less than five, is accomplished at a high angle of attack (initially 38 degrees) during which the blanketing effect of the wing essentially precludes any rudder control. Coordinated lateral-directional control is provided by combined yaw reaction control jets and aileron control. The terminal phase occurs as angle of attack is reduced below 18 degrees. As the orbiter descends to altitudes where winds can result in relatively large errors in inertially derived air data, probes are extended (M=3.5) to provide air data relative to the vehicle. During a typical normal entry, range control is achieved by bank angle while angle of attack follows a predetermined schedule to achieve (at approximately M = 1.5) an angle somewhat smaller than that corresponding to maximum L/D. A downrange capability of up to 7,960 kilometers with a cross range capability of 1,815 kilometers may be realized. Subsonic flight is achieved at an altitude of approximately 12,190 meters. Range control during the gliding descent is obtained by angle of attack modulation with velocity control maintained by the speed brake. The approach and landing interface occurs at 3,048 meters above ground level and a preflare is initiated at an appropriate altitude, followed by a deceleration float and touchdown. The initial approach target and flare altitude will be scheduled to provide a minimum of 25 seconds between flare initiate and touchdown. Touchdown occurs at an angle of attack of about 15 degrees. The nominal touchdown velocity is 88 meters/sec, and maximum landing speed with a 14,515-kilogram payload is about 106 meters/sec including dispersions for hot-day effects and tailwinds.

Orbiter Aerodynamic Criteria

Aerodynamic criteria, Reference 1, for the orbiter vehicle require the configuration to perform as both a spacecraft and an aircraft. Because of this, the external features must be carefully configured to provide the protection and versatility required for orbital and atmospheric flight, and the aerodynamic performance and control necessary for unpowered descent and landing. The aerodynamic lines must ensure performance that is acceptable over the hypersonic to subsonic speed range, and provide the required cross range capability and touchdown velocity. Aerodynamic requirements, Table 2, were developed from analysis of the entry phase of the mission. Landing requirements are shown in Figure 6. Static stability was not required since the design criteria allowed reliance on the flight control system to meet flying qualities criteria. Early simulations identified a flight control requirement for static longitudinal stability to be no more than two percent body length (5.45 percent mean aerodynamic chord) unstable so the pitching moment curve established the aft center of gravity limit at 67.5 percent of body length. Payload criteria established a center of gravity range of 2.5 percent, thus establishing the forward limit.

The selected configuration, Figure 2, evolved from a series of program and technical refinements directed to achieve the vehicle yielding the best combination of performance and cost. This evolution is discussed further in a later section. The double-delta planform combined with a moderately low fineness ratio (approximately five) body minimizes interference heating effects, provides the required cross range requirements, and possesses an acceptable trim and stability range, Figure 7, over the flight Mach number range.

The orbiter wing was sized to provide a 88 meters/second touchdown speed (V_D) at a 15-degree angle of attack (tail scrape attitude for main gear strut compressed, tire flat) with body flap retracted and the center of gravity at the forward limit. The leading edge sweep (45 degrees) and aspect ratio (2.265) were selected on the basis of aerothermodynamic trade studies to provide the design touchdown speed for a center of gravity at the forward limit with minimum wing size and to optimize the wing leading edge thermal protection system for a reuse cycle of 100 flights prior to major rework.

The fuselage was designed to accommodate a variety of payloads and house the crew and maneuvering control systems. Nose camber, cross section, and upward sloping forebody sides were selected to improve hypersonic pitch trim and directional stability and in conjunction with wind-body blending, to reduce entry heating on the body sides. Propulsion units for entry attitude control and orbital maneuvering have been incorporated in pods located in the aft body fairings. The body flap is used to protect the Shuttle main engine during entry and to provide trim capability to relieve elevon loads.

The vertical tail has been sized to provide a low-speed C_{n_β} of 0.0013 at an angle of attack of 13 degrees about a center of gravity located at the aft limit. It has a reference area of 38.39 m^2 including the rudder/speed brake. The rudder is split along the orbiter buttock plane to provide

directional stability augmentation in the hypersonic/supersonic flight regimes and to apply drag modulation for the subsonic flight phases, approach and landing. The section profile is a five-degree, half-angle, 60-40 double-wedge airfoil.

Aerodynamic and aerothermodynamic criteria, Reference 2, regarding surface discontinuities, thermal protection system tile steps and gaps, and waviness are shown in Figure 8. These criteria are based on aerodynamic efficiency requirements of lifting surfaces and the prevention of premature transition from laminar to turbulent boundary layers in the high heating portion of entry. Aerodynamic efficiency is affected to a much greater extent by surface conditions of the forward rather than aft regions of components. Hence, tolerance criteria are generally more restrictive for forward regions of the vehicle surfaces and somewhat relaxed at aft portions.

DEVELOPMENT APPROACH

Development Schedule

Major program milestones are illustrated in Figure 9, starting with authority to proceed (ATP) in 1972 and culminating with initial operational capability in 1980. The orbiter concept at ATP was a blended delta wing vehicle based on precontract studies and configured to meet initial Shuttle Program requirements. As a result of a continuing assessment of system requirements and technical refinements, early in the contract the orbiter concept was modified to reduce weight and decrease program and operating costs (Reference 3). As discussed in more detail later, refinements in the aerodynamic configuration led to a double-delta planform incorporating a more efficient lifting surface than the blended delta. The System Requirements Review in August 1973 finalized technical requirements for the Space Shuttle systems (i.e., the total vehicle, its elements, and their ground systems) and approved the design approach of the vehicle and associated support equipment. Preliminary Design Review (PDR) of the first orbiter (Orbiter 101) vehicle and subsystems for the approach and landing flight test program was completed in February 1974, followed by the Preliminary Design Review of the second orbiter (102) in March 1975. Orbiter 101 roll-out from final assembly in Palmdale, California, took place in September 1976. The vehicle was mated to the Boeing 747 carrier aircraft at the Dryden Flight Research Center, Edwards Air Force Base, and the first captive flight was completed in February 1977. The first airlaunch of Orbiter 101 for the approach and landing flight test (ALT) took place on August 12, 1977, and the final flight was completed on October 26, 1977. Delivery of OV101 to the Marshall Space Flight Center, Alabama, for ground vibration testing took place in March 1978. Fabrication and assembly of Orbiter 102, the first orbital vehicle, began in 1975. Rollout is scheduled for late 1978, followed by delivery to Kennedy Space Center, Florida, and first manned orbital flight in 1979. The first six orbital flights of the Shuttle are development test flights, and the seventh flight in 1980 is considered the initial operational capability flight.

Aerodynamic Design Approach

It is conventional in an aircraft program to approach flight demonstration by incremental expansion of the flight envelope. This is not feasible with the Shuttle vehicle. Once Shuttle is launched, it is committed to flight over the complete mission profile from ascent to orbiter insertion, deorbit, entry, and landing. Flight characteristics must be based on aerodynamic data derived from ground testing and analysis. Careful attention has been given to the interactions between flight control systems design and aerodynamic characteristics, and allowance has been made for uncertainties in basic aero data in flight control design. Predicted aerodynamic characteristics have been derived from extensive wind tunnel tests which have included a systematic investigation of data uncertainties, nonlinear effects, and effects of wind tunnel installation, blockage, and shock wave reflections. The Langley Research Center conducted detailed wind tunnel investigations of control surface characteristics and nonlinear aerodynamic effects, (i.e., Reference 4) to support development of the data base.

Wind Tunnel Program

Key to Space Shuttle development has been the acquisition of wind tunnel test data to support design and evaluation by providing a continuously maturing data base reflecting configuration and subsystem updates. By first orbital flight in 1979, approximately 40,100 total wind tunnel test hours will have been conducted for aerodynamics, heat transfer, and structural dynamics, consisting of approximately 20,200 for the orbiter vehicle, 16,100 for the mated launch configuration, and 3,800 for the carrier aircraft program, Table 3. A total of 94 models have been built—38 aerodyamic, 36 heat transfer, and 20 structural dynamic, Table 4. All wind tunnel testing is coordinated with and approved by NASA management at JSC.

In order to accurately simulate flight conditions in a wind tunnel, Reynolds number and Mach number must be matched. Problems in flow simulation (Reference 5, NASA CP-2009) occur when the geometric scaling of viscous flow is important, or when coupling between the viscous surface flow and the external flow field is strong. In the first case, the boundary layer can be considered separately from the inviscid flow field, and viscous effects can be scaled. This holds for Mach numbers up to about 10. It is well known, for example, that skin friction varies with Reynolds number in a predictable manner and can be scaled to flight conditions from suitable wind tunnel results.

For Mach numbers greater than about 10, a pressure interaction results from the outward streamline deflection induced by a thick boundary layer, and the viscous-inviscid interaction can no longer be neglected. For this case, there are two classical simulation parameters commonly considered:

(1) $\bar{x}_\infty$, the viscous interaction parameter introduced by Hayes and Probstein (Reference 6)

$$\bar{x}_\infty = \frac{M_\infty^3 \sqrt{C'_\infty}}{\sqrt{Re_{\infty_x}}} \tag{1}$$

(2) $\bar{V}'_\infty$, the viscous parameter introduced by Whitfield and Griffith (Reference 7)

$$\bar{V}'_\infty = \frac{M_\infty \sqrt{C'_\infty}}{\sqrt{Re_{\infty_x}}} \tag{2}$$

where M_∞ is the freestream Mach number, C'_∞ is the factor of proportionality in the linear viscosity-temperature relation (Reference 8), and Re_{∞_x} is the freestream Reynolds number based on x. The parameter $\bar{x}_\infty$ is the relevant parameter for the "pressure" in both the strong and weak interaction cases; whereas $\bar{V}'_\infty$ is the relevant parameter in terms of "pressure coefficient" (i.e., $\bar{x}_\infty/q_\infty$). For Shuttle, it has been observed that $\bar{V}'_\infty$ correlates total aerodynamic coefficients better than $\bar{x}_\infty$, and consequently, $\bar{V}'_\infty$ has been used as the hypersonic simulation parameter.

Figure 10 shows a comparison between flight Re and $\bar{V}'_\infty$ and the simulation capability of typical wind tunnels used to develop the Orbiter aerodynamic data base. It is seen that the tunnel capabilities closely match flight simulation requirements.

Orbiter aerodynamic test hours are summarized in Figure 11 which illustrates the phasing and relationship to program milestones, and the distribution by speed range. Approximately 38 percent of the hours were utilized in subsonic test, 44 percent in the transonic/supersonic range, and 18 percent in the hypersonic testing. Four test phases will be completed by first orbital flight. The first was a configuration definition phase to develop wing airfoil section and planform geometry in support of design trades to reduce orbiter weight which led to selection of the double-delta arrangement. This phase was completed by System Requirements Review in August 1973. The second phase extending essentially to OV102 Preliminary Design Review in March 1975 was dedicated to refinement of the orbiter vehicle and development of the ferry flight configuration. A tailcone configuration was developed to improve ferry performance and provide longer duration orbiter flights during the approach and landing test program. Orbiter tests were conducted to determine basic stability and control capability over the complete entry speed range. Control surface effectiveness and hinge moments were measured to support preliminary design and sizing of actuators. Initial RCS interaction tests were conducted to support entry control analysis. Tests were also performed to measure Reynolds number and viscous interaction effects and to identify wind tunnel sting tare corrections to test data. In addition, the Langley Research Center conducted testing to measure orbiter damping derivatives.

The third phase of the test program was implemented following OV102 Preliminary Design Review in March 1975 to provide more detailed OV102 design data and to verify the aerodynamic characteristics of OV101 prior to first captive flight in February 1977. The Langley Research Center program to investigate nonlinear aerodynamic and control surface interaction characteristics was continued during this phase. In addition, extensive testing was conducted to develop the orbiter air data system and provide sensor calibrations for both OV101 and 102. OV101 verification testing was also completed during this period utilizing a 0.36-scale model in the Ames Research Center 40x80-ft (12.2x24.4 m) wind tunnel. This model was an accurate replica of the actual OV101 flight vehicle and incorporated simulated thermal protection system tiles, outer moldline protuberances, and main engine and reaction control system exhaust nozzles.

The final phase, initiated in early 1978, is still in progress and is directed toward verification of OV102 characteristics prior to first orbital flight. Two models are employed (0.05 and 0.02 scale) to cover the speed range from Mach 16 to 0.2. Figure 12, illustrates the details of protuberances, cavities, and thermal seals simulated on the models.

Aerodynamic Uncertainties

Allowance has been made for uncertainties in basic aerodynamic data used in design of the Shuttle Vehicle, subsystems, and early mission profiles, Reference 9. Two categories of uncertainties have been defined: 1) Tolerances, which account for wind tunnel data accuracy and manufacturing tolerances; and 2) Variations, which account for unknowns in extrapolation of model data to free-flight. "Tolerances" are used in subsystem design, and were derived from a statistical analysis of wind tunnel data in which tests were conducted using the same models in several different wind tunnels and using different scale models in the same wind tunnel. "Variations" are used in establishing flight test plans and constraints, and were determined from comparisons between predicted aerodynamics and flight test results from lifting entry vehicles and selected high-speed aircraft. The flight data will allow reductions of the variations and removal of corresponding flight placards to achieve operational capability.

A multiple regression analysis computer program, Reference 10, was used to determine the "tolerances" on the derivatives C_L, C_D, C_m versus α; C_n, C_ℓ versus β, δ_a, and δ_r. Utilization of the program involved inputting available sets of wind tunnel data for a specified coefficient versus α, β, δ_a or δ_r at given conditions of Mach number, control surface setting, etc., with a proposed form of curve-fit; e.g., $C_L = K_0 + K\alpha + K_2\alpha^2 - \ldots K_5\alpha^5$. The regression program statistically determines which terms of the proposed

curve-fit equation are significant and eliminates those which are not significant by performing a least-square curve-fit of the test data. Subsequent to selecting a "best" curve-fit, the deviation of each test point from the curve is computed and the Standard Error of estimate, S_e, (which is a measure of the standard deviation, σ) is multiplied by three to estimate the three-sigma (3σ) tolerance of the aerodynamic coefficient, C, being analyzed. The three-sigma tolerance is an increment or band about a nominal value of the aerodynamic coefficient, C, for any given Mach number, body flap deflection, etc., where the probability that a measured coefficient at the specified condition lies within C $\pm 3\sigma$ is 99.73 percent. An example of the procedure for determining the tolerance on lift coefficient is shown in Figure 13. The regression program yields a polynominal expression for lift coefficient in terms of angle of attack:

$$C_L = -0.0546 + 0.0178\,\alpha + 0.0003\,\alpha^2 - 2 \times 10^{-9}\,\alpha^5$$

The standard error of estimate becomes $S_e = 0.0146$ and the corresponding three-sigma tolerance on lift coefficient at Mach 5.0 becomes 0.0438.

"Variations" were developed for three speed regimes from comparisons of flight and predicted values based on wind tunnel test data for representative vehicles, constructing the bounds of the data points and applying the larger bound as a plus or minus value. An example of the procedure used to develop variation uncertainties is displayed in Figure 14. The figure presents a comparison between predictions based on wind tunnel results and flight measured values of normal force for selected aircraft and space vehicles. The data bands were selected on the basis of engineering judgment and weighting "Shuttle-like" configurations more heavily than the lifting bodies. The speed regime groups were $M \leq 0.8$, $0.8 \leq M \leq 1.2$ and $M \geq 1.2$. The ratio of variation to tolerance at Mach 10.0 was assumed to apply throughout the viscous interaction speed region.

Later in this report where Orbiter flight data from the approach and landing test program are discussed, comparisons are shown between estimated tolerances and variations for several aerodynamic parameters. The measured flight test data points are seen to be distributed about the nominal value and to fall within the predicted tolerance band, and well within the estimated variations. It is anticipated that further correlation with flight data will permit reduction of the variations and removal of corresponding flight placards to achieve full operational capability.

CONFIGURATION EVOLUTION

Stability, control, and performance requirements for aerodynamic configuration design of the orbiter vehicle are, for the most part, established by the entry and recovery phases of flight. Consequently, it is these phases of flight which were key in determining aerodynamic requirements for the orbiter external arrangement. On the other hand, design airload conditions are primarily determined from the ascent phase.

Design issues key to achieving the proper aerodynamic balance to provide stability, control, and center of gravity range capability across the entry/recovery flight regime are wing design, wing-body integration, and integration of aerodynamic and flight control requirements. Wing design was key because of its influence on vehicle weight, thermal environment, aerodynamic stability, buffet characteristics, and gliding and landing performance capability. Wing-body integration was important in obtaining a balanced aerodynamic configuration capable of trim and control over the entire speed range, and in minimizing thermal environment due to interference flow effects. Fuselage dimensions were largely fixed by payload size and packaging efficiency while aerodynamic and aerothermodynamic considerations established forebody shape and local contours. Integration of aerodynamic control requirements was of major importance in meeting flying quality goals in all flight regimes, and minimizing vehicle weight as affected by control surface arrangement, size, and actuator requirements.

Prior to Shuttle Program go-ahead in August 1972, Rockwell International participated in extensive NASA-funded Shuttle System studies during which numerous trades (Reference 1) were conducted to determine Shuttle operational cost effectiveness, desired configuration and geometry, major subsystem definition, and identification of major design drivers for the orbiter configuration. Design requirements found to be key configuration drivers are landing speed; payload size, weight, and center of gravity envelope; entry cross range and aerodynamic heating; stability and control requirements; and flying qualities. From these studies emerged a basepoint configuration at Shuttle Program authority to proceed (ATP). Following ATP, further trade studies were conducted at NASA/JSC and Rockwell to refine the basepoint design. Essentially four aerodynamic basepoints were evaluated in arriving at the final selected design, as summarized in Figure 15.

ATP Configuration

For the ATP orbiter aerodynamic configuration, Rockwell selected a blended delta wing-body design to meet NASA mission requirements. Selection of the external arrangement was based on results of previous investigations at the NASA centers, and Rockwell design studies, supported by 4300 hours of wind tunnel testing. The orbiter aerodynamic shape incorporated a 50-degree swept delta wing planform sized to provide 77.2 m/sec design touchdown speed with 18,100 kilograms return payload. Hypersonic L/D was 1.3 at 34-degree angle of attack, and maximum subsonic L/D was 5.7. Elevons were sized to provide trim at hypersonic speeds over an angle of attack range from 20 to 50 degrees with an operational center of gravity range of three percent body length. The cargo bay provided a 4.57 meter diameter by 18.2 meter long volume for a wide variety of payloads. Cargo deployment/retrieval manipulators were stowed in a dorsal fairing along the top of the payload bay doors. Provision was made for installing four airbreathing engines in the aft portion of the payload bay for early development flights. Three main propulsion system rocket engines were located at the base of the aft fuselage, and on-orbit propulsion engines were installed

in two removable pod modules alongside the aft fuselage. Reaction control rocket engines were located in the aft pods and in the forward fuselage compartment.

PRR - PDR Configuration

Upon initiation of Shuttle go-ahead, the development aerodynamic wind tunnel program was implemented, and further trade studies were conducted at NASA/JSC and Rockwell to refine the ATP basepoint. The ATP and PRR orbiters (Figure 15) were both blended delta wing configurations which were externally similar. The most obvious changes were: (1) a redesigned forebody to accommodate internal packaging revisions; (2) the movement of the OMS/RCS pod from the side of the aft fuselage to the shoulder location; and (3) deletion of airbreathing propulsion for landing assist following orbital flights.

A series of wind tunnel tests conducted over the Mach number range from 0.26 to 7.4, indicated revised wing twist, camber, and fuselage blending would improve low-speed lift capability. Results showed that reducing the wing-body fillet radius and changing from a faired to a straight fillet (wing-glove) increased the trim C_L significantly. In addition, significant system requirement changes were made by NASA to reduce vehicle weight and cost. Orbiter down payload weight was reduced from 18,100 to 11,300 kilograms, and the vehicle resized from a design dry weight of 77,100 kilograms to 68,000 kilograms. The minimum subsonic stability requirements were reduced from three percent to 0.5 percent body length static margin at the forward center of gravity. For the PDR configuration, Reference 3, direction was received from NASA to modify the wing planform to a double-delta design, and the wing was resized to meet the reduced dry weight and payload requirements. A 45/79 degree wing planform with reduced glove leading edge radius was incorporated for improved subsonic performance, Figures 16 and 17. Improved low-speed performance and the reduced static margin requirement permitted a reduction in wing size from 299 to 250 square meters and resulted in rebalancing the orbiter vehicle to meet stability and control requirements.

CDR Configuration

Wind tunnel investigations of the PDR configuration revealed a need for further configuration refinement. Aerodynamic tests showed a difficulty in providing trim capability at the forward center of gravity in the supersonic flight regime. Aeroheating tests indicated the blunt fuselage nose resulted in early transitional flow and high temperatures along the lower body surface. Also, wing incidence, camber, and thickness distributions designed for maximum subsonic performance led to local fairings on the lower wing and fuselage surfaces which caused high local heating.

Changes incorporated in the fuselage nose section are illustrated in Figure 18. The blunt nose shape was modified to a cross section which was basically parabolic in plan and side-view. Wing/fuselage fairings along the bottom of the orbiter were modified to provide a thermodynamically aceptable smooth lower surface with minimum reverse curvature, Figure 19. Leading edge sweep of the glove was slightly changed (from 78 to 81 degrees) as a result of refairing into the modified fuselage nose.

To achieve the best combination of performance and cost, further configuration refinements were made. The down payload requirement was increased to 14,500 kilograms and the design center of gravity range established at 2.5 percent body length. The OMS pod forebody fairing which extended onto the cargo bay door was shortened to reduce weight and simplify the door-to-fuselage seal design. In addition, the manipulator arm dorsal fairing along the top of the payload bay doors was deleted, and the manipulator was stowed inside the payload bay, Figure 20. Aerodynamic criteria for the final configuration are listed previously in Table 2.

ORBITER AERODYNAMIC CHARACTERISTICS

Aerodynamics characteristics of the final orbiter vehicle, Reference 2, are summarized in this section. These characteristics were derived from wind tunnel test results adjusted to account for scale effects or differences between model configurations and the final orbiter vehicle. Aeroelastic corrections have been estimated by standard methods. Wind tunnel skin friction drag and reaction control rocket plume interaction data have been corrected to free-flight conditions using Reynolds number scaling for skin friction, and jet-to-freestream-momentum ratio for plume effects.

Criteria for aerodynamic design of the Orbiter have been determined from analyses of the entry flight phase, considering requirements for vehicle trim, control, performance, and aerodynamic heating. A typical entry profile is illustrated in Figure 21. Trajectory guidance is accomplished by flying an angle of attack/velocity profile preselected to meet thermal design criteria, and using roll commands for range control. Flight control is accomplished in two modes termined spacecraft and aircraft. The spacecraft mode applies from initial through mid-entry phases where the Orbiter is at high angle of attack making the vertical fin and rudder ineffective. The aircraft mode includes mid-entry through approach and landing. Switching from spacecraft to aircraft modes is performed as a function of angle of attack and velocity. Transition begins at approximately Mach 5 and is completed at about Mach 1.5. In the spacecraft mode, control in all three axes is initially provided by the aft reaction control system jets mounted at the base of the Orbiter on either side of the vertical tail. As control authority of the aerodynamic surfaces becomes sufficient, the jets are deactivated. Utilization of the control surfaces and jets during entry is illustrated in Figure 22. At a dynamic pressure of 95.8 N/m^2, the elevons are used to supplement the jets in pitch and roll. The roll jets are turned off at a dynamic pressure of 478.8 N/m^2 at which point the yaw jets are used to initiate roll maneuvers (as well as yaw control) with the ailerons providing turn coordination until switchover to the aircraft mode. At a dynamic pressure of 957.6 N/m^2, the pitch jets are turned off and the elevons provide pitch control. Transition to the aircraft mode is initiated at approximately Mach 5 when the rudder is activated. The yaw jets are turned off at about Mach 1, and the

rudder provides control until landing. The speed brake is programmed to assist pitch trim and augment lateral stability during transition from spacecraft to aircraft control. During approach and landing, the speed brake setting is modulated for speed control. Additional pitch trim is provided by the body flap which is programmed as a function of velocity.

Significance of the aerodynamic parameters rests in their effects on vehicle performance, control, and airloads. Those parameters most sensitive to meeting entry mission requirements are listed in Table 5. Lift, drag, and pitching moment are the primary aerodynamic parameters governing the entry trajectory, range capability, and thermal system design requirements in terms of heat rate and load. Heating rate influences maximum surface temperature and affects material reuse capability. Heat load establishes material thickness to maintain structural temperatures and, therefore, affects thermal protection system weight. Pitching moment determines the elevon setting required for trim. Design areas sensitive to trim setting are elevon heating during initial entry, and control surface actuator stall limits at transonic speeds. In addition, there is an interaction between elevon setting and lateral-directional control capability because of the change in roll and yaw effectiveness of the ailerons with elevon position. Lateral-directional trim and control capability is governed by the aileron and rudder control derivatives. Above Mach 5 the aileron is used for both roll and yaw trim before the rudder become effective. Between Mach 5.0 and 1.5, the rudder provides both yaw and roll trim with the aileron providing turn coordination. Below Mach 1.5, roll trim is provided by the rudder. The derivatives C_{n_β}, C_{ℓ_β}, $C_{n_{\delta_a}}$, $C_{\ell_{\delta_a}}$, $C_{n_{\delta_r}}$, $C_{\ell_{\delta_r}}$ are key to establishing control capability, reaction control system propellant usage, and the switch-over point from spacecraft to aircraft control modes.

High Altitude Aerodynamics

The entry interface, defined as the upper limit of the sensible atmosphere, begins at approximately 120,000 meters altitude. In this high altitude region, say 70,000 to 120,000 meters, rarefied gas flows are encountered by the orbiter as it enters the atmosphere. Aerodynamic design issues in this region involve determining the effectiveness of the control jets and their influence on the Orbiter flow field, in addition to defining viscous interaction effects associated with low Reynolds number/high Mach number flows.

Initial entry aerodynamic characteristics, Figure 23, are highly influenced by interactions between the reaction control system jet plumes and the local flow field over the Orbiter. The total jet effects are comprised of three factors:

- Jet thrust
- Surface impingement
- Flow field interaction

Impingement and interaction effects are inter-related and have been obtained from wind tunnel testing. Coupling is present between the plume effects and aero surfaces, and between the jets themselves.

A series of model nozzles with different expansion ratios were employed during the wind tunnel test program. General Dynamics/Convair, under contract to the NASA (NAS9-14095), Reference 11, developed a method whereby the experimentally measured induced plume effect (surface impingement plus flow field interaction) could be separated into two component parts and the impingement term extrapolated to flight conditions. To obtain a correct modeling of the reaction control system plume effects in the wind tunnel, it was necessary to observe certain scaling criteria. The primary factors for consideration, aside from dimensional scaling, are plume shape and jet-to-freestream momentum ratio, ϕ_j/ϕ_∞. In some instances, namely, yaw thruster firings, mass flow rate ratio, $\dot{m}_j/\dot{m}_\infty$, scaling was found to be a slightly better modeling parameter than momentum ratio. The scaling parameters are defined as:

$$\frac{\phi_j}{\phi_\infty} = \frac{m_j\, v_j}{2\bar{q}_\infty\, S_{ref}}\, n = 7.3879\, \frac{n}{\bar{q}_\infty} \tag{3}$$

and

$$\frac{\dot{m}_j}{\dot{m}_\infty} = \frac{\phi_j}{\phi_\infty}\, \frac{v_\infty}{v_j}\, \frac{1}{n}\, (\sin\theta_j)^{1/2} = 1.300 \times 10^{-3}\, \left(\frac{v_\infty}{\bar{q}_\infty}\right) \tag{4}$$

where

$\dot{m}_j$ = Jet mass flow rate

$\dot{m}_\infty$ = Freestream mass flow rate

v_j = Exit velocity ~ meters/sec

$\bar{q}_\infty$ = Dynamic pressure ~ N/m^2

θ_j = Nozzle half-angle at exit

n = Number of thrusters

S_{ref} = Reference area (24.9 m^2)

In scaling from wind tunnel to flight, certain adjustments to the data base are required to account for real exhaust plume effects since cold air was used as the jet media in the tunnel. Model plume impingement effects were theoretically extracted from the measured tunnel data and the remaining jet plume interaction effects correlated against ϕ_j/ϕ_∞ or $\dot{m}_j/\dot{m}_\infty$. Prototype impingement effects were then theoretically generated. Examples of the data correlation for pitching moment are presented in Figure 24.

The application of the reaction control system data to a typical entry flight condition of $\bar{q}_\infty$ = 478.8 N/m^2 at an altitude of 79,250 meters are presented in Figure 25 for three aft left downfiring reaction control system thrusters. It is to be noted that adverse effects to control authority result from the impingement and flow interaction terms for roll and pitch; whereas, in yaw these terms tend to increase the jet moment.

Viscous interaction effects are scaled from wind tunnel test data to flight conditions by means of the hypersonic viscous parameter $\bar{V}'_\infty$ discussed earlier:

$$\bar{V}'_\infty = M_\infty \sqrt{\frac{C'_\infty}{Re_{\infty_{L_B}}}} \tag{2}$$

where

M_∞ = Freestream Mach number

$Re_{\infty_{L_B}}$ = Freestream Reynolds number (based on body length, L_B)

C'_∞ = Proportionality factor for the linear viscosity-temperature relationship (Reference 8)

$$= \left[\frac{T'}{T_\infty}\right]^K \left[\frac{T_\infty + 122.1 \times 10^{-(5/T_\infty)}}{T' + 122.1 \times 10^{-(5/T')}}\right] \tag{5}$$

with Monahan's empirical relationship given by

$$\frac{T'}{T_\infty} = 0.468 + 0.532 \frac{T_W}{T_\infty} + 0.195 \frac{\gamma - 1}{2} M_\infty^2 \tag{6}$$

where

T' = Reference temperature, degrees Kelvin

T_∞ = Freestream static temperature, degrees Kelvin

T_W = Wall temperature, degrees Kelvin

γ = Specific heat ratio

K = Empirical constant = 0.5 for air

j = Empirical constant = 1.0 for air

NOTE: A constant wall temperature of 1367°K and specific heat ratio of 1.15 have been assumed for the flight conditions analyzed.

The primary viscous interaction effects are in shear forces with essentially no effect on normal force. Variation of $\bar{V}'_\infty$ along the nominal entry trajectory is illustrated in Figure 26. High values of $\bar{V}'_\infty$ correspond to low values of Reynolds number which is associated with the thickening of the hypersonic laminar boundary layer causing increased shear on the lower surface of the Orbiter. Evidence of this is seen as an increase in axial force coefficient with increasing $\bar{V}'_\infty$ with no change in normal force, Figure 27. Pitching moment at zero degree control deflection, Figure 28, becomes slightly more negative with increasing $\bar{V}'_\infty$ due to increased shear forces on the lower surface of the Orbiter. At negative (trailing edge-up) control deflections, the movement of the control surface has little effect on the boundary layer on the lower surface of the Orbiter, and consequently, the effect of $\bar{V}'_\infty$ on pitching moment is similar to the zero degree deflection case. For positive (trailing edge-down) deflections, however, the pitching moment effectiveness of the control surface decreases with increasing $\bar{V}'_\infty$. At high $\bar{V}'_\infty$ (corresponding to low Reynolds number) a thickening of the boundary layer results with a separation point which moves forward with increasing control deflection. This causes a net forward movement of the center of pressure, resulting in reduced pitching moment effectiveness with increasing $\bar{V}'_\infty$, Figure 28.

Effects of $\bar{V}_\infty'$ on aerodynamic performance characteristics are indicated in Figures 29 and 30 for a nominal entry trajectory. The decrease in lift-to-drag ratio caused by the increase in axial force is accounted for in design of the entry trajectory. Reduced elevon effectiveness increases the control surface deflection required to trim, Figure 30.

Longitudinal Characteristics

Longitudinal stability and control characteristics for hypersonic to low speed Mach numbers are illustrated in Figures 31 and 32. These data have been determined as a result of extensive wind tunnel tests (representative data are shown on the curves) with hypersonic theory being used to bridge the gap between high supersonic data and the hypersonic wind tunnel data. Low-speed longitudinal characteristics shown in Figure 32 demonstrate stall-free characteristics over the operating angle of attack range. The predicted characteristics are compared with test data obtained with a 0.36-scale model in the Ames Research Center 40x80-ft (12.19x24.38 m) wind tunnel. The changes in stability evidenced in Figure 32 by the large changes in pitching moment at high angles of attack are due to leeside separation on the orbiter wing induced by vortices from the wing/fuselage junction.

The leeside flow separation influences the supersonic stability characteristics also. Referring to Figure 31, it can be seen that for M = 10 and 5, the variation of pitching moment with normal force coefficient for zero and positive elevon deflection follows the classical Newtonian "sine squared" relationship. This relationship between pitching moment and normal force coefficient does not follow the "sine-square" variation for negative elevon deflections. The change in characteristics is due to the change in flow pattern on the leeside of the Orbiter wing as influenced by negative elevon deflections.

The surface flow patterns on the leeside of the Orbiter wing consist of three distinct flows. At low angles of attack, the flow which is initially perpendicular to the leading edge is turned parallel to the freestream by the presence of the fuselage (Figure 33A). When the angle of attack is great enough to cause the wing leading edge shock to detach, the trailing edge shock will become strong enough to separate the boundary layer (Figure 33B). This separation is the result of subsonic flow aft of the detached shock expanding around the leading edge and reattaching at supersonic speeds. The flow must still be turned into the freestream direction as before. The turning is accomplished by a strong shock that causes the boundary layer to separate. The wake begins to affect the flow pattern at higher angles of attack causing a secondary type of separation (Figure 33C). Leeside flow boundaries for M = 6.0 are shown in Figure 34. The relationship between spanwise location of the shock induced separation $\frac{b_s}{b}$, and Mach number was obtained from a correlation of delta wing data. The shock detach boundary was obtained from oil flow photographs.

The effect of leeside separation on wing pitching moment is shown in Figure 35. The subsonic leading edge suction that occurs when the bow shock detaches results in a more stable pitching moment slope. The change to a more stable slope is the result of leading edge suction when the wing bow wave detaches and a reduction of lift over the wing area aft of separation line (Figure 35). The center of pressure is more aft for the lift gain (due to leading edge suction) than for the lift loss due to shock-induced pressure aft of the separation line. The wing pitching moment becomes more stable, thus accounting for the increased stability shown in Figure 31 for +10-degrees elevon deflection.

Elevon effectiveness is also influenced by leeside separation. Loss in elevon effectiveness at high negative (trailing edge up) deflection can be attributed to the effect of back-pressure on the leeside flow field. Flap type controls will often cause boundary layer separation, especially in hypersonic low-density flows. Such back-pressure effects are of practical concern since it is desirable to control the Orbiter with leeward control deflection (trailing edge up) in order to minimize control surface heating. Figure 36 shows elevon effectiveness data obtained from the AEDC Tunnel A at M = 5 for an elevon deflection -35 degrees. The measured elevon effectiveness is seen to be less than shown by shock expansion theory. This is probably due to shock-induced separation. The separation extent increases with angle of attack. After the angle of attack for shock detachment is reached, the back-pressure effect from the elevon will affect the wing flow. At high angles of attack, the positive lift produced by the wing vortices outweighs the negative lift generated by the elevon-induced flow separation over the inner wing surface. The result is a loss of elevon effectiveness below the shock expansion value. Adjusting the theory for leeside separation results in reasonable agreement between theory and experiment.

Static trim capability for the elevon and body flap positioned for trim to the forward and aft center of gravity positions is displayed in Figure 37. The control schedules presented on the figure are for determining maximum obtainable center of gravity trim limits. A reserve for maneuvering, trimming spanwise center of gravity offset, manufacturing misalignments, and aerodynamic uncertainties has been added to the limits of the elevon effectiveness data to establish the limits shown on the figure. The aft center of gravity limits are based on a positive elevon deflection of 15 degrees for Mach numbers less than or equal to ten. A positive elevon deflection of ten degrees was used for Mach numbers greater than ten due to thermal protection system design limits during maximum heating conditions. Forward center of gravity trim limits are based on an incremental pitching moment coefficient reserve of 0.015 for Mach numbers less than or equal to ten and 0.02 for Mach numbers greater than ten. Figure 37 indicates a slightly reduced forward center of gravity trim margin at Mach 5.0 in the angle of attack range from 20 to 45 degrees. This is attributed to the loss in elevon effectiveness due to leeside separation. Center of gravity trim limits for the entry angle of attack schedule have been shown earlier in Figure 7. Both Figures 7 and 37 indicate that a wide trim margin exists across the Mach number range.

Elevon control power in conjunction with the body flap and speed brake provide trim capbility between the design center of gravity limits. The elevon schedule, shown in Figure 38, illustrates the nominal and the most positive and negative settings for trim at forward and aft center of gravity positions. The extreme settings account for control margin and uncertainties in aerodynamic characteristics. The speed brake is initially opened during entry at Mach 10, and is programmed as a function of velocity to

approximately Mach 1. Opening the speed brake at Mach 10 assists in longitudinal trim during the transition from high to low angle of attack. Below Mach 1, the speed brake setting is modulated to provide speed control during approach and landing. The body flap is used as a trim device to keep the elevons operating in an effective range, and, during the high heating portion of entry, to keep the elevons from overheating. Body flap deflection varies during entry. For entry at the forward center of gravity, the initial body flap position is normally full-up. For the aft center of gravity case, the initial position is approximately 16 degrees down.

Lateral-Directional Characteristics

Lateral-directional stability and control characteristics along the nominal entry trajectory are illustrated in Figures 39, 40, and 41. As shown in Figure 39, the Orbiter exhibits positive dihedral effect (negative C_{ℓ_β}) across the complete Mach range during both the spacecraft and aircraft control modes. During the spacecraft mode, and during transition to the aircraft mode, the directional stability derivative C_{n_β} is negative. C_{n_β} becomes positive indicating static stability in yaw at approximately Mach 1.7, and retains positive values throughout the aircraft mode (Mach numbers below approximately 1.5). Aileron and rudder control effectiveness characteristics are illustrated in Figures 40 and 41. Because the ailerons provide control authority across the complete Mach range, and the rudder is essentially ineffective above Mach 8, the ailerons are used in conjunction with the yaw jets to provide for roll control in the spacecraft control mode.

Early analytical studies predicted an elevon deflection interaction effect on the lateral-directional characteristics. Studies showed that the relatively large sized elevon in the presence of the deep, flat-sided fuselage could induce a change in the pressure distribution in the aft region of the fuselage. The resulting change in pressure distribution resulted in an incremental change in side force, yaw, and rolling moment when the vehicle was yawed. The effect of elevon interaction is illustrated for the yawing and rolling moment derivatives in Figures 42 and 43. The control derivatives $C_{\ell_{\delta_a}}$ and $C_{n_{\delta_a}}$ are also affected by elevon position. The influence of elevon position on the control derivatives is shown in Figures 44 and 45. The sensitivity of the derivatives to elevon position influences vehicle control boundaries.

The nature of the control derivatives define the Mach regions where aileron and/or rudder is used for lateral trim. Aileron-alone is used for Y_{CG} trim above Mach number 4.5 and rudder-alone is used for Y_{CG} trim below Mach number 3.5. A combination of aileron and rudder control is used for trim in the Mach number region between 4.5 and 3.5. The yaw reaction control system (RCS) jets are used to augment the aerodynamic controls where required.

The interrelation between the control derivatives and the method used to trim Y_{CG} offset during the spacecraft mode is best illustrated by examining the relations for aileron and rudder required to trim. Using aileron-alone:

$$\delta A_{trim} = \frac{Y_{CG}}{b} \frac{C_N C_{n_\beta} + C_A C_{\ell_\beta}}{C_{\ell_\beta} C_{n_{\delta_a}} - C_{n_\beta} C_{\ell_{\delta_a}}} \tag{7}$$

and for rudder-alone:

$$\delta R_{trim} = \frac{Y_{CG}}{b} \frac{C_N C_{n_\beta} + C_A C_{\ell_\beta}}{C_{\ell_\beta} C_{n_{\delta_r}} - C_{n_\beta} C_{\ell_{\delta_r}}} \tag{8}$$

The critical boundary exists when the denominator goes to zero; i.e., the condition where aileron or rudder cannot produce a trim condition.

For aileron-alone, the boundary is defined by

$$C_{\ell_\beta} C_{n_{\delta_a}} - C_{n_\beta} C_{\ell_{\delta_a}} > 0, \quad \frac{C_{n_\beta}}{C_{\ell_\beta}} > \frac{C_{n_{\delta_a}}}{C_{\ell_{\delta_a}}} \tag{9}$$

Using rudder-alone:

$$C_{\ell_\beta} C_{n_{\delta_r}} - C_{n_\beta} C_{\ell_{\delta_r}} > 0, \quad \frac{C_{n_\beta}}{C_{\ell_\beta}} > \frac{C_{n_{\delta_R}}}{C_{\ell_{\delta_r}}} \tag{10}$$

Aileron and rudder cross coupling ratios are shown in Figure 46 for the nominal entry trajectory and nominal aerodynamics. For the spacecraft control mode, the boundary for Y_{CG} trim by aileron control is not violated for Mach numbers greater than about 1.9. Trim of a Y_{CG} offset by rudder-alone can be accomplished over the region from Mach 8 to approximately 1.1, resulting in an overlap from Mach 8 to 1.9 for nominal

aerodynamics. To allow for trajectory dispersions and uncertainties in aerodynamics, transition to the aircraft control mode; i.e., conventional aileron/rudder control, is initiated at approximately Mach 5 and is complete by Mach 1.5.

Low-speed directional stability characteristics exhibit a strong Reynolds number/angle of attack effect, Figure 47. The figure illustrates the importance of full-scale Reynolds number testing on high angle of attack aerodynamics. Test data obtained from models tested at low Reynolds numbers ($\leq 5 \times 10^6$ based on mean aerodynamic chord) show essentially no change of directional stability with angle of attack. The early work of Polhamus (Reference 12) and Jorgensen and Brownson (Reference 13) indicated that Reynolds number and body corner radius could have a significant effect on the high angle of attack characteristics of the Orbiter. These predictions were borne out when the Orbiter model was tested at near full-scale Reynolds number in the Ames Research Center 40x80-foot (12.2x24.4 m) wind tunnel. Referring to Figure 47, it can be seen that the high Reynolds number test data shows a decrease in directional stability with angle of attack which is in contrast to the low Reynolds number data which shows essentially no change in stability with angle of attack. At Mach numbers above 0.7, data representative of flight Reynolds numbers can be obtained in wind tunnel tests at low Reynolds numbers provided proper attention is paid to close matching of body corner rounding on the wind tunnel models and flight vehicles (Reference 13).

The early work of E.C. Polhamus (Reference 12) was used to predict the variation of directional stability with angle of attack. Based on Polhamus' work, it was determined that the low-speed/high angle of attack directional stability determined by wind tunnel tests would be erroneous unless the Reynolds number were sufficiently high to permit proper simulation of the cross flow on the forward fuselage. It was predicted that a close similarity in both magnitude and change with Reynolds number, existed between the cross flow drag coefficient for the Orbiter fuselage at high angles of attack (greater than 15 degrees) and a two-dimensional square cylinder at 90 degrees angle of attack. From this similarity, it was concluded that most of the low-speed Orbiter test data would be within the critical Reynolds number range, the range in which cross flow drag coefficient decreases from high to low values as the Reynolds number increases from subcritical to critical. Polhamus presented data from tests made on noncircular cylinders with the air flow directed normal to the cylinder axis. As illustrated in Figure 48 for a square-shaped cylinder with rounded corners, the air flow will separate on the leeside at subcritical Reynolds number but will remain attached at supercritical Reynolds number, when the flow is directed at an angle not aligned with one of the major cross sectional axes. For the subcritical Reynolds number case, the resultant body axis side force, C_Y, is positive while for the supercritical Reynolds number case, the side force is negative. Since the center of gravity is behind the nose, positive side force translates to positive yawing moment and negative side force translates to negative yawing moment. Consequently, the effect of going from subcritical to supercritical Reynolds number is to reduce the directional stability of the vehicle.

Presented in Figure 49 is the measured directional stability variation with cross flow Reynolds number from several wind tunnel tests at approximately 20 degrees angle of attack. As can be seen, there appears to be a trend for the Orbiter directional stability to decrease as the cross flow Reynolds number is increased. The reason for the reduction of directional stability with increased cross flow Reynolds number is the elimination of the flow separation at the nose with increased cross flow Reynolds number. At angles of attack of 15 degrees and below (Figure 47), there appears to be no change of directional stability for the different tests.

FLIGHT TEST RESULTS

The Approach and Landing Test (ALT) Program, Table 6, was conducted during the last half of 1977 as part of the Shuttle Development Program. The Orbiter Enterprise (OV101) was launched from the Boeing 747 Shuttle Carrier Aircraft over Edwards Air Force Base, California, and glided to either a landing on Rodgers Dry Lake, or on the last flight, a landing on the Edwards Air Force Base runway. The program conconsisted of eight captive flights followed by three orbiter freeflights with the tailcone installed, and finally two freeflights in which the tailcone was removed, testing the orbital return configuration.

The captive flights verified the airworthiness of the mated configuration, accomplished Orbiter systems checkout and developed the separation procedures, and verified aerodynamic forces at separation. The separation of the Orbiter from the 747 was achieved through the aerodynamic forces on the vehicles, so one of the important objectives of the Captive Flight Program was to verify the predicted separation forces, and adjust the Orbiter elevon settings for separation, if required. Special load cells were installed on the Orbiter/747 struts in order to measure the separation forces to the required accuracy.

The orbiter lift and pitching moments in the presence of the 747 were the key parameters for safe separation. Figure 50 shows these coefficients as determined during the captive flights using load cell measurements, compared to estimates based on wind tunnel tests. The flight measured coefficients were well within the uncertainties in the prediction. Since dynamic analyses had shown acceptable separations if the key aero coefficients were within the uncertainty band, the flight measurements confirmed that separation would be acceptable, and the program proceeded to an Orbiter freeflight. The first separation occurred on August 12, 1977, and was as predicted.

The first three Orbiter freeflights were conducted with a tailcone installed to fair the Orbiter's blunt base. The tailcone provided increased glide range by increasing the Orbiter L/D from a maximum of 4.5 to 7.5. It also allowed increased launch altitude, from 6400 m to 7620 m. The tailcone also was intended to reduce buffet levels at the 747 empennage, since there was some concern that with the Orbiter tailcone-off, the Orbiter wake may induce excessive buffeting and reduce the 747 fatigue life. (Flight measurements of fluctuating structural loads in the 747 tail later relieved this concern.)

After three tailcone-on freeflights, the tailcone was removed and the test program completed with the orbital configuration simulated. Two Orbiter freeflights were accomplished with the tailcone removed. These flights obtained the data used to verify the subsonic aerodynamic characteristics of the Orbiter in its orbital return configuration. Separation of the orbiter/747 during the first tailcone-off freeflight is illustrated in Figure 50. In Figure 51, the orbiter is shown just prior to touchdown on the runway at Edwards Air Force Base during the final freeflight on October 26, 1977.

The significant Orbiter aerodynamic characteristics are compared with predictions based on wind tunnel tests, Figures 52 through 56. Key instrumentation used to derive these data were an "Aerodynamic Coefficient Identification Package" provided by the NASA/Dryden Flight Research Center, consisting of three accelerometers and three rate gyros, and a flight test noseboom which provided angles of attack and sideslip, and pitot and static pressures. A data extraction program was developed by the NASA to determine the flight-derived aerodynamic characteristics (Reference 14). The figures show that the flight measurements were in good agreement with wind tunnel predictions, with the lone exception of landing gear drag which was overpredicted by approximately 27 percent. Examination of the wind tunnel data revealed that the estimated Reynolds number correction to gear drag was inadequate. Thus, the aerodynamics objective of the Approach and Landing Test Program; to verify the low-speed aerodynamic characteristics, was achieved and provided increased confidence for the next phase of the Shuttle Program, the Orbital Flight Test.

CONCLUSIONS

Aerodynamic development of the Space Shuttle orbiter has been described. Extensive wind tunnel testing has provided a high confidence level in the estimated aerodynamic characteristics. Results from the approach and landing flight test program verify predicted aerodynamic characteristics in the subsonic speed regime. Accounting for uncertainties in aerodynamic data will allow incremental extension of flight envelopes to achieve predicted operational capability.

REFERENCES

1. Surber, T.E. and Olsen, D.C., "Space Shuttle Orbiter Aerodynamic Development," Journal of Spacecraft and Rockets, Vol. 15, No. 1, January-February 1978, pp 40-47

2. Rockwell International Space Division, "Aerodynamic Design Data Book, Volume 1, Orbiter Vehicle," November 1977, Report No. SD 72-SH-0060-1K

3. Smith, E.P., Rockwell International Space Division, "Space Shuttle Orbiter and Subsystems," June 1973, Report No. SD 72-SH-0144

4. Gamble, Joe D., Chrysler Corporation Space Division, "High Supersonic Stability and Control Characteristics of a 0.015-Scale (Remotely Controlled Elevon) Model 49-O of the Space Shuttle Orbiter Tested in the NASA/LaRC 4-Foot UPWT (LA63B)," May 1976, Report No. DMS DR-2279, NASA CR-144.606

5. NASA LaRC, "High Reynolds Number Research," October 1976, Report No. NASA CP-2009, pp 2-17

6. Hayes, Wallace D., and Probstein, Ronald F., "Hypersonic Flow Theory," New York and London, Academic Press, 1959, pp 333-345

7. Whitfield, Jack D., and Griffith, B.J., "Hypersonic Viscous Drag Effects on Blunt Slender Cones," AIAA Journal, Vol. 2, No. 10, October 1964, pp 1714-1722

8. Bertram, Mitchell H., NASA, "Hypersonic Laminar Viscous Interaction Effects on the Aerodynamics of Two-Dimensional Wedge and Triangular Planform Wings," August 1966, Report No. NASA TN D-3523

9. Rockwell International Space Division, "Aerodynamic Design Substantiation Report, Volume 1, Orbiter Vehicle," February 1978, Report No. SD 74-SH-0206-1K

10. Stein, Robert E., Jr., Lockheed Electronics Inc., "Project 3313, Multiple Regression Analysis Program for the Aerodynamic Coefficient Analysis System (NASA Contract NA9-122000)," January 1973

11. Rausch, J.R., General Dynamics Convair Division, "Space Shuttle Orbiter Rear Mounted Reaction Control System Jet Interaction Study," May 1977, Report No. CASD-NSC-77-003

12. Polhamus, E.C., "Effect of Flow Incidence and Reynolds Number on Low Speed Aerodynamic Characteristics of Several Noncircular Cylinders with Application to Directional Stability and Spinning," NASA Technical Report R-29, 1959

13. Jorgenson, Leland H. and Brownson, Jack J., "Effect of Reynolds Number and Body Corner Radius on Aerodynamic Characteristics for Space Shuttle-Type Vehicle at Subsonic Mach Numbers," NASA TN D-6615, January 1972

14. Romere, P.O., Eichblatt, D.L., Underwood, J.M., and Howes, D.B., "The Space Shuttle Orbiter Approach and Landing Tests—A Correlation of Flight and Predicted Performance Data," AIAA Paper 78-793, AIAA Tenth Aerodynamic Testing Conference, San Diego, CA, April 19-21, 1978

ACKNOWLEDGEMENTS

The aerodynamic design activities described in this report are being accomplished by the Space Division, Rockwell International, under NASA contract NAS9-14000. Overall technical management of orbiter development is accomplished by the Space Shuttle Program Office at the NASA Johnson Space Center (JSC). Aerodynamic development is directed by JSC through the Space Shuttle Flight Performance Technical Management area, Mr. Bass Redd, Technical Manager, supported by Mr. James C. Young, Aerodynamic Subsystem Manager. In addition to JSC, the other NASA Centers (Ames Research Center, Langley Research Center, and Marshall Space Flight Center) have provided extensive support to the Shuttle development in accomplishment of the Wind Tunnel Program and in analysis of test results. In addition, the Langley Research Center has provided additional program support through their independent investigations of nonlinear aerodynamics.

At Rockwell, significant contributions to this paper have been made by Messrs. D.C. Olsen, H.S. Dresser, W.R. Russell and L.M. Gaines.

Table 1 BASELINE REFERENCE MISSIONS

MISSION	LAUNCH SITE	OBJECTIVE	INCL. (DEG)	ORBIT ALTITUDE (10^3 m)	ORBIT DURATION (DAYS)	PAYLOAD (10^3 Kg) ASCENT	PAYLOAD (10^3 Kg) DESCENT
1	KSC	PAYLOAD DELIVERY	28.5	277.8	7	29.48	14.51
2	KSC	COMBINED REVISIT TO ORBITING ELEMENT & SPACELAB	55.0	500.0	7	---	---
3A	WTR	PAYLOAD DELIVERY	104.0	185.2	1 REVISIT	14.51	1.13
3B	WTR	PAYLOAD DELIVERY	104.0	185.2	1 REVISIT	1.13	11.33

Table 2 AERODYNAMIC DESIGN REQUIREMENTS

PARAMETER	VALUE
ANGLE OF ATTACK	
HYPERSONIC	25 DEG TO 50 DEG
TRANSONIC	0 DEG TO 15 DEG
SUBSONIC	-5 DEG TO 20 DEG
CENTER OF GRAVITY RANGE	
MINIMUM TRAVEL	2% BODY LENGTH
DESIGN RANGE	0.65 L_B - 0.675 L_B
LANDING PERFORMANCE	
PAYLOAD	14,515 Kg
LANDING WEIGHT (WITH PAYLOAD)	85,230 Kg
MINIMUM DESIGN TOUCHDOWN SPEED, V_D	88 m/sec
LONGITUDINAL STABILITY	
MINIMUM HYPERSONIC STATIC MARGIN	POSITIVE
MINIMUM SUBSONIC STATIC MARGIN (AFT CENTER OF GRAVITY)	-2% L_B (-5.45% MAC)
LIFT/DRAG MODULATION	
PEAK SUBSONIC VALUE (GEAR-UP, δ_{SB} = 0)	NOT LESS THAN 4.4
PEAK SUBSONIC VALUE (GEAR-UP, δ_{SB} = 85 DEG	NOT LESS THAN 2.5

Table 3 SPACE SHUTTLE WIND TUNNEL TEST HOURS SUMMARY AUGUST 1972 TO FIRST ORBITAL FLIGHT

	ORBITER VEHICLE	MATED LAUNCH VEHICLE	CARRIER AIRCRAFT	TOTAL HOURS
AERODYNAMICS	14,700	8,100	3,400	26,200
AERODYNAMIC HEATING	4,500	6,400	0	10,900
STRUCTURAL DYNAMICS	1,000	1,600	400	3,000
TOTAL	20,200	16,100	3,800	40,100

Table 4 SPACE SHUTTLE WIND TUNNEL MODEL SUMMARY AUGUST 1972 TO FIRST ORBITAL FLIGHT

	NUMBER OF MODELS			
	ORBITER VEHICLE	MATED LAUNCH VEHICLE	CARRIER AIRCRAFT	TOTAL
AERODYNAMICS	11	23	4	38
AERODYNAMIC HEATING	22	14	0	36
STRUCTURAL DYNAMICS	12	6	2	20
TOTAL	45	43	6	94

Table 5 SIGNIFICANT AERODYNAMIC PARAMETERS

AERODYNAMIC PARAMETERS	FLIGHT REGIME	WHY PARAMETERS ARE SIGNIFICANT	AERO CONCERN IN DEFINITION OF PARAMETERS
L/D	ALL	• CROSS RANGE • TERMINAL AREA ENERGY MANAGEMENT • ELEVON TO TRIM • RCS FUEL USAGE	• VISCOUS INTERACTION EFFECTS • FLOW SEPARATION • REAL GAS EFFECTS NOT DUPLICATED IN WIND TUNNEL
C_M, $C_{M_{\delta_E}}$			
HINGE MOMENTS	TRANSONIC MACH 0.9 TO 1.5	• DESIGN HINGE MOMENT CONDITIONS • DEFINES CONTROL SURFACE STALL CONDITIONS	• TRANSONIC WIND TUNNEL DATA ACCURACIES
$C_{n_{\delta_a}}$, $C_{\ell_{\delta_a}}$	MACH 5 TO 6	• AILERON USED FOR BOTH ROLL & YAW TRIM ABOVE MACH 5 BEFORE RUDDER BECOME EFFECTIVE • YAW JET FUEL USAGE (DUE TO CG OFFSET)	• CONTROL SURFACE INTERACTION
$C_{n_{\delta_a}}$, $C_{\ell_{\delta_a}}$, $C_{n_{\delta_r}}$, $C_{\ell_{\delta_r}}$	HIGH SUPERSONIC MACH 3 TO 5 SUPER/TRANSONIC MACH 2.5 TO 1.0	• BETWEEN MACH 1.5 TO 5, RUDDER IS USED FOR BOTH YAW & ROLL TRIM. AILERON COORDINATES TURN • YAW JET NEEDED UNTIL RUDDER IS EFFECTIVE • DEFINES SWITCH-OVER POINT	• CONTROL SURFACE INTERACTIONS • RUDDER EFFECTIVENESS AT HIGH α, MACH • AEROELASTIC EFFECTS • TRANSONIC WIND TUNNEL DATA ACCURACIES

Table 6 APPROACH & LANDING TEST PROGRAM SUMMARY

	NO. OF FLIGHTS	CONFIGURATION	OBJECTIVE
CARRIER ALONE	4	MODIFIED 747	FUNCTIONAL CHECK, FLUTTER, & STALL CHECKS
	7	MODIFIED 747 WITH ORBITER ATTACH STRUCTS & TIP FINS	FLUTTER CLEARANCE, PERFORMANCE, & STABILITY & CONTROL VERIFICATION
CAPTIVE FLIGHT	5	747 & ORBITER, TAILCONE-ON, ORBITER UNMANNED & UNPOWERED	FLUTTER CLEARANCE, PERFORMANCE, & STABILITY & CONTROL VERIFICATION
CAPTIVE ACTIVE	3	747 & ORBITER, TAILCONE-ON, ORBITER MANNED & POWERED-UP	ORBITER FUNCTIONAL CHECK, SEPARATION LOADS, & PROCEDURES VERIFICATION
ORBITER FREE-FLIGHT	3	TAILCONE-ON	CREW FAMILIARIZATION, SYSTEMS CHECK, STABILITY & CONTROL, & PERFORMANCE VERIFICATION
	2	TAILCONE-OFF	VERIFICATION OF ORBITER APPROACH & LANDING CAPABILITY
CAPTIVE INERT	4	FERRY CONFIGURATION, TAILCONE-ON	FERRY QUALIFICATION & PERFORMANCE VERIFICATION

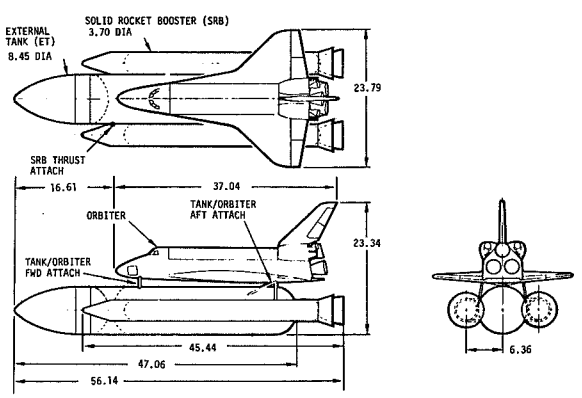

Fig. 1 SPACE SHUTTLE VEHICLE

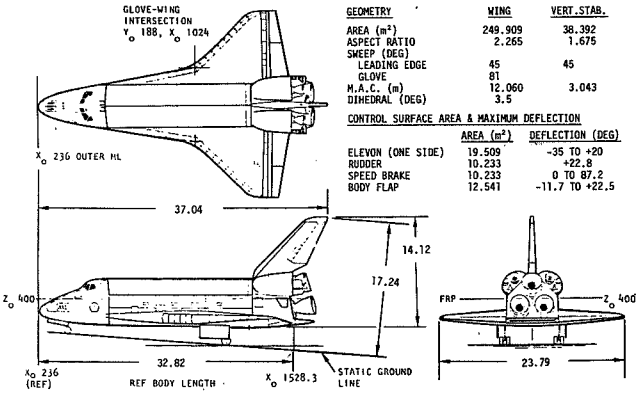

Fig. 2 ORBITER VEHICLE

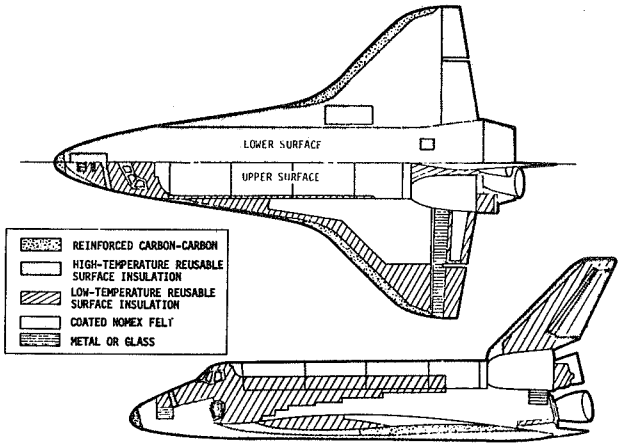

Fig. 3 THERMAL PROTECTION SUBSYSTEM

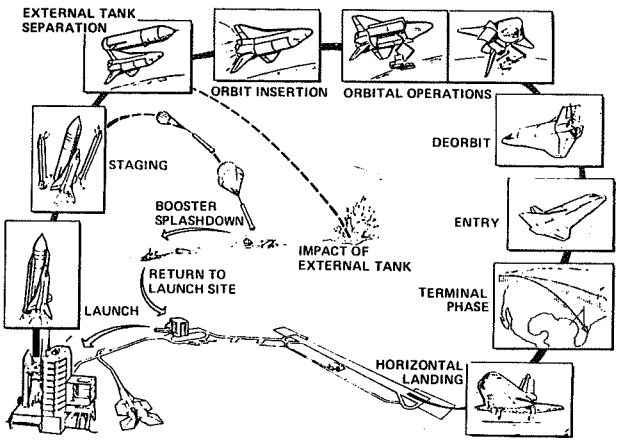

Fig. 4 SHUTTLE MISSION PROFILE

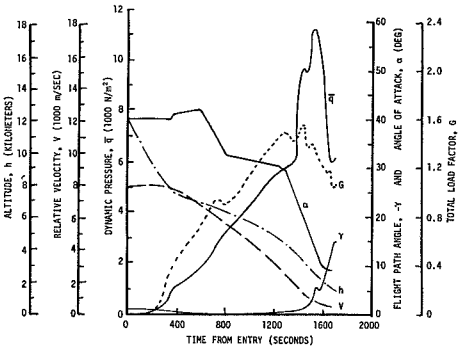

Fig. 5 ORBITER ENTRY TRAJECTORY

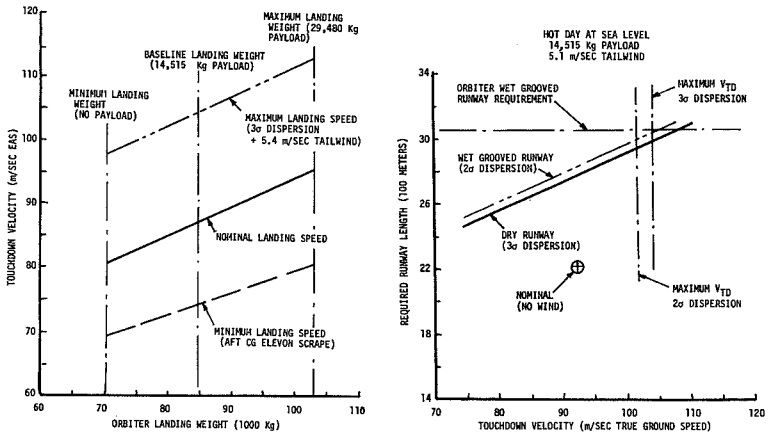

Fig. 6 LANDING REQUIREMENTS

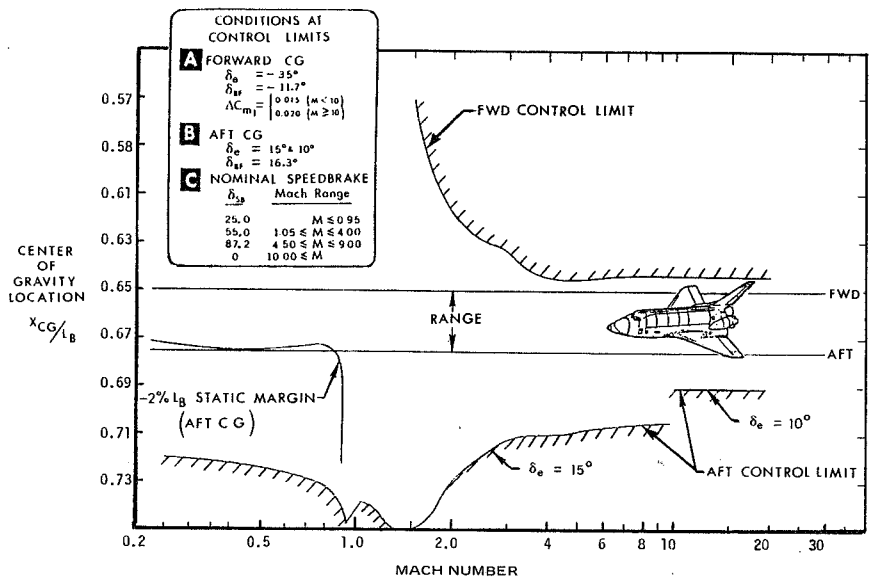

Fig. 7 ORBITER TRIM LIMITS

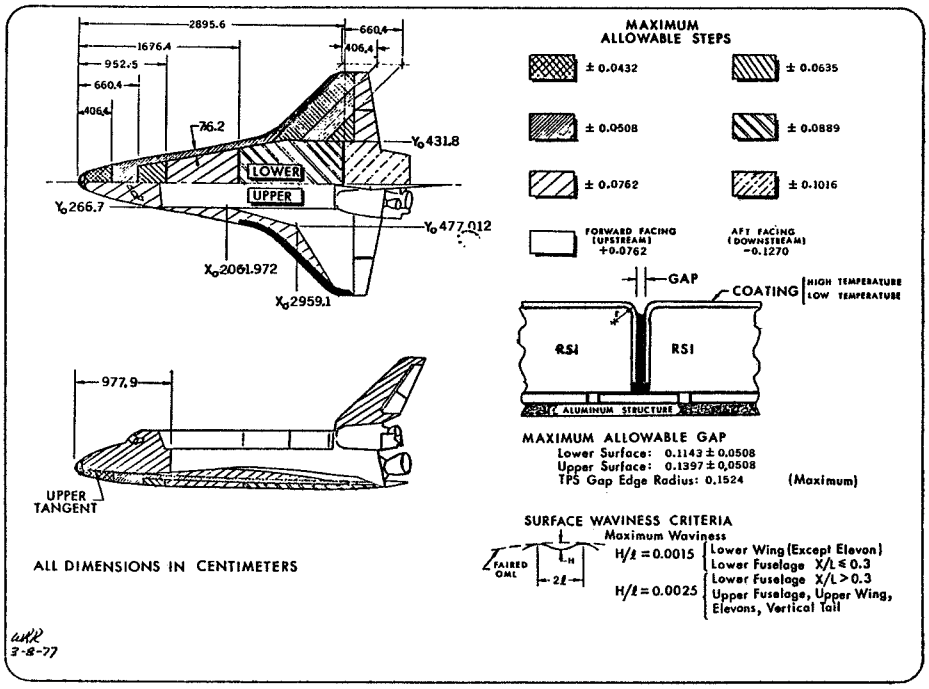

Fig. 8 ORBITER MOLD LINE/STEP CRITERIA

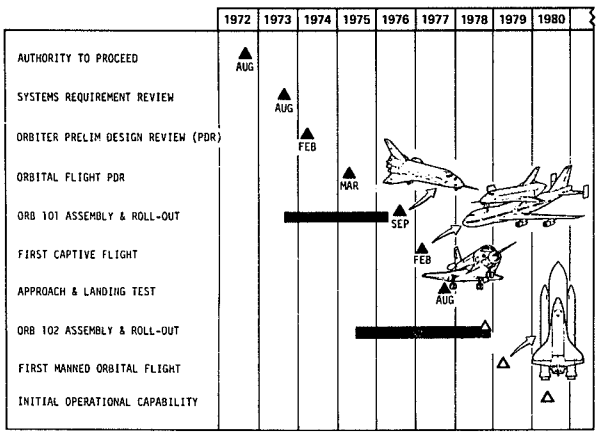

Fig. 9 SPACE SHUTTLE PROGRAM MILESTONES

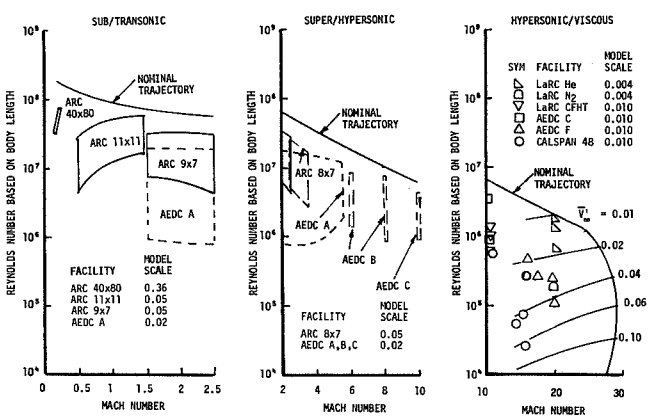

Fig. 10 ORBITER FLIGHT REYNOLDS NUMBER SIMULATION

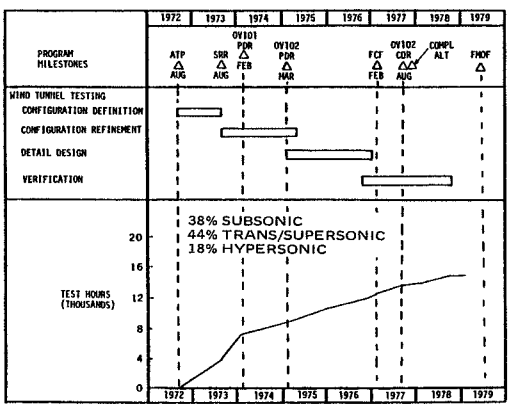

Fig. 11 ORBITER AERODYNAMIC WIND TUNNEL PROGRAM

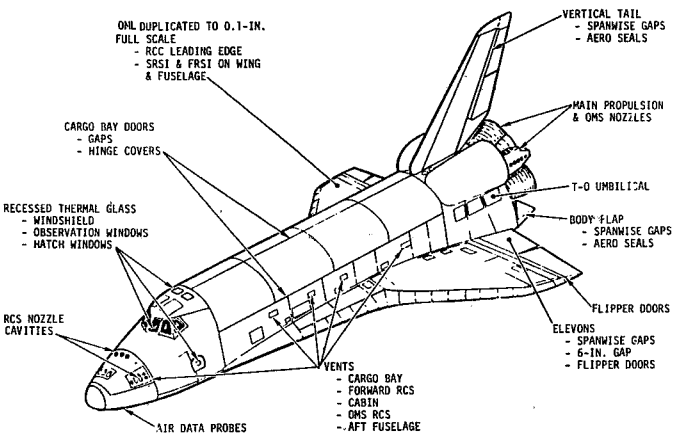

Fig. 12 OV102 MODEL FIDELITY

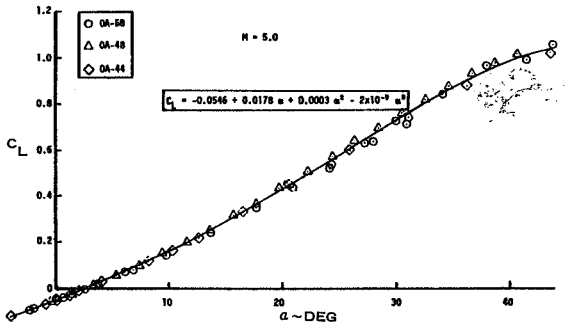

Fig. 13 LIFT COEFFICIENT TOLERANCES

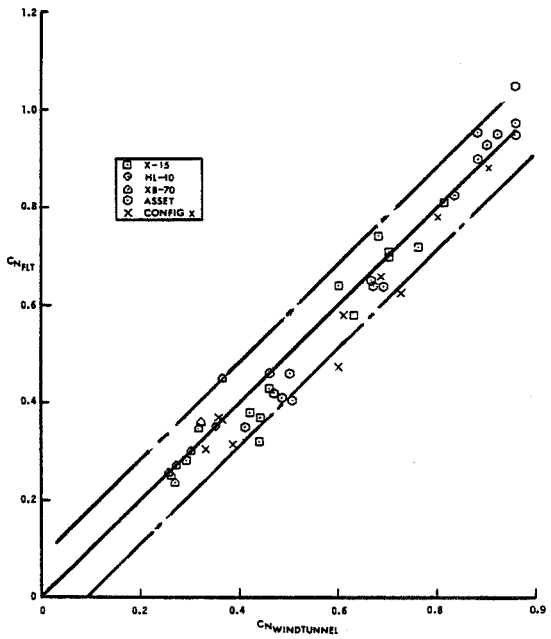

Fig. 14 NORMAL FORCE COEFFICIENT COMPARISON OF WIND TUNNEL TO FLIGHT DATA

CONFIGURATION NUMBER	ATP	PRR	PDR	CDR
WING PLANFORM	50° BLENDED DELTA	50° BLENDED DELTA	45°/79° DBL DELTA	45°/81° DBL DELTA
PROFILE	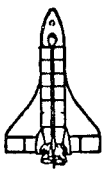	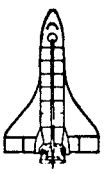	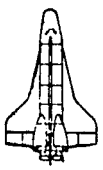	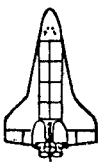
DRY WEIGHT (Kg)	77,110	77,110	68,039	68,039
PAYLOAD (Kg)	18,144	18,144	11,340	14,515
CG RANGE % L_B	65-68	65-68	65-67.5	65-67.5
WING AREA (m^2)	299.15	299.15	249.91	249.91
WING SPAN (m)	25.60	25.60	23.80	23.80
OVERALL LENGTH (m)	37.79	38.10	38.10	37.28

Fig. 15 ORBITER EVOLUTION SUMMARY

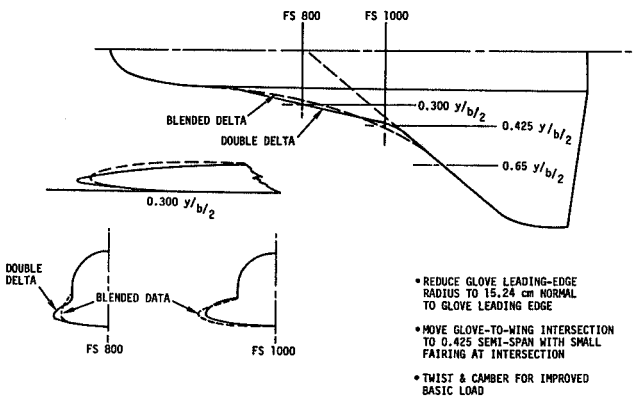

Fig. 16 BLENDED/DOUBLE-DELTA WING MODIFICATION

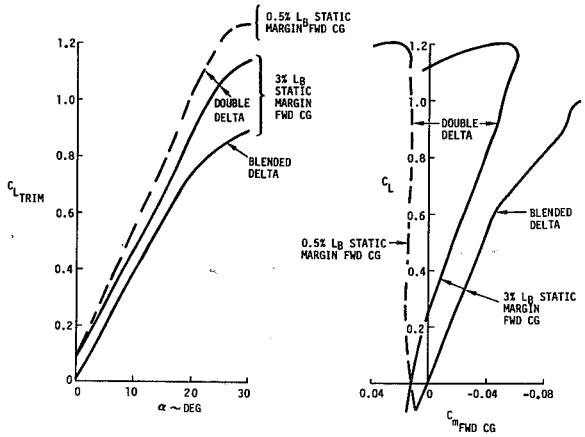

Fig. 17 BLENDED/DOUBLE-DELTA WING MODIFICATION EFFECT ON LONGITUDINAL CHARACTERISTICS

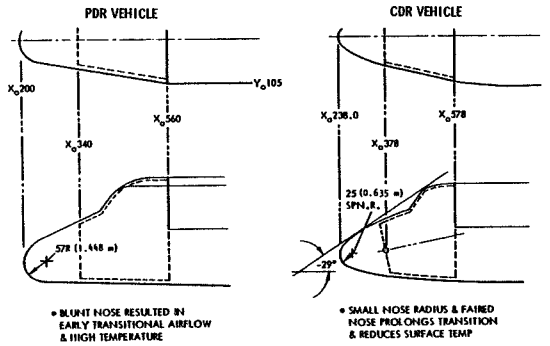

Fig. 18 REDUCED NOSE RADIUS AND REFAIRED NOSE SECTION

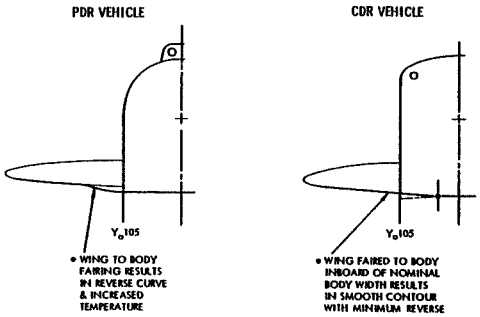

Fig. 19 LOWER WING/BODY FAIRING

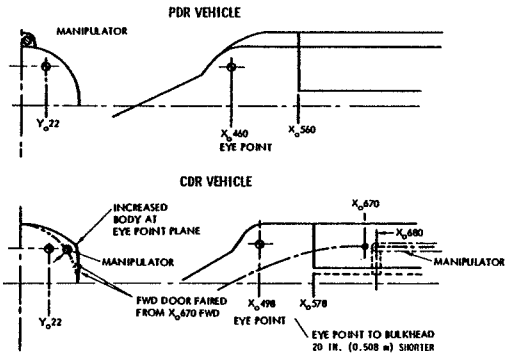

Fig. 20 UPPER BODY LINES

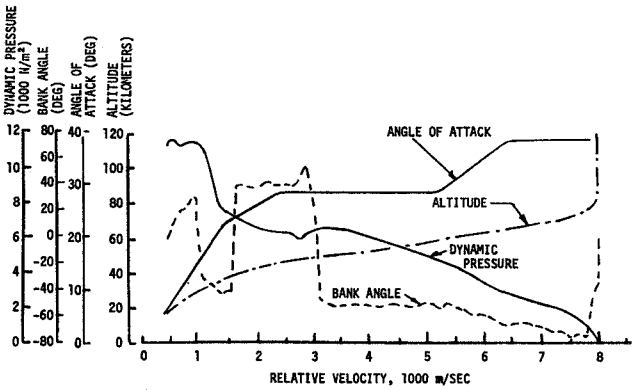

Fig. 21 TYPICAL ORBITER ENTRY PROFILE

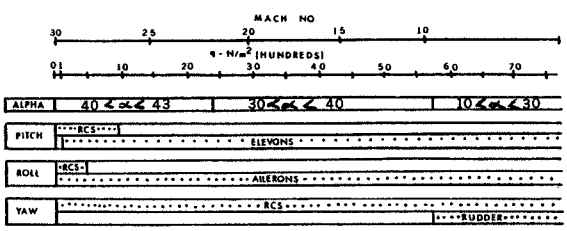

Fig. 22 RCS AND CONTROL SURFACE UTILIZATION DURING ENTRY

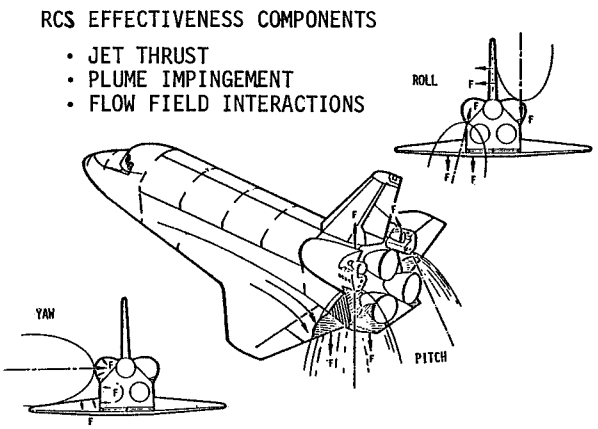

Fig. 23 REACTION CONTROL JET INTERACTIONS

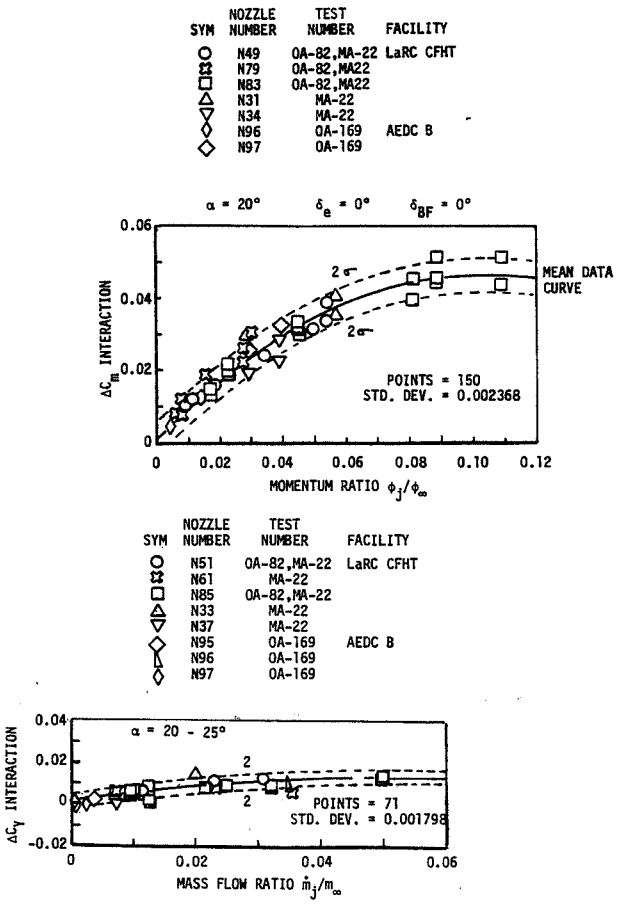

Fig. 24 REACTION CONTROL JET CORRELATION

$\alpha = 20°$ $\beta = 0°$ $\delta_E = \delta_{BF} = 0°$ $\bar{q}_\infty = 47.9$ N/m²

CONTROL AXIS	3-JET MOMENT (N-m)	IMPINGEMENT MOMENT (N-m)	INTERACTION MOMENT (N-m)	NET MOMENT (N-m)
ROLL	+36,590	-8,030	-27,040	+1,520
PITCH	-126,600	+8,690	+43,775	-74,135
YAW	-38,300	-7,860	-4,860	-51,020

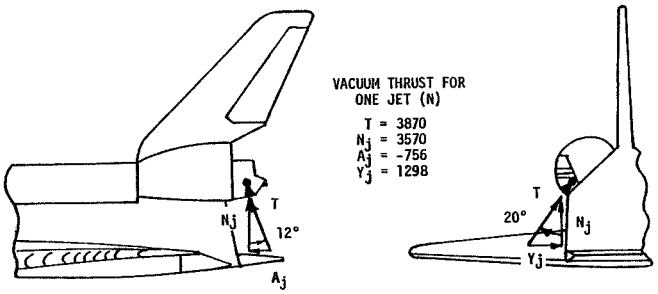

Fig. 25 REACTION CONTROL JET MOMENTS

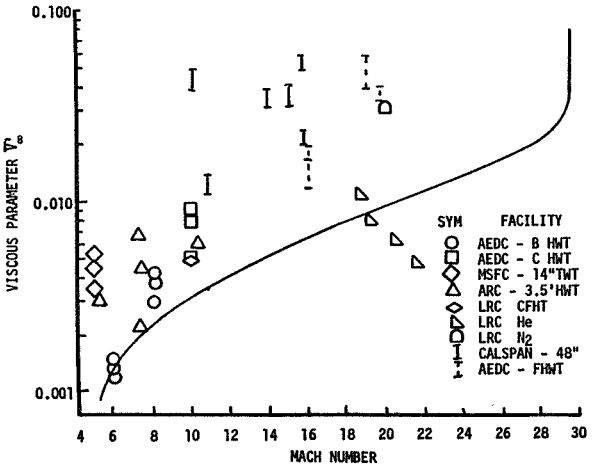

Fig. 26 VARIATION OF VISCOUS PARAMETER ALONG NOMINAL ENTRY TRAJECTORY

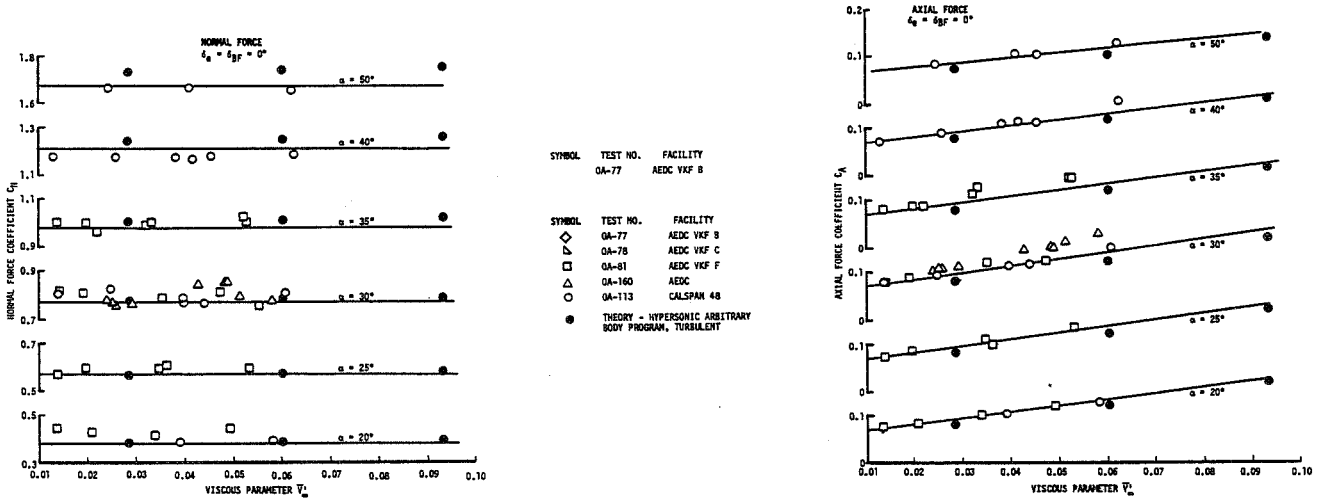

Fig. 27 EFFECTS OF VISCOUS INTERACTION ON NORMAL AND AXIAL FORCE

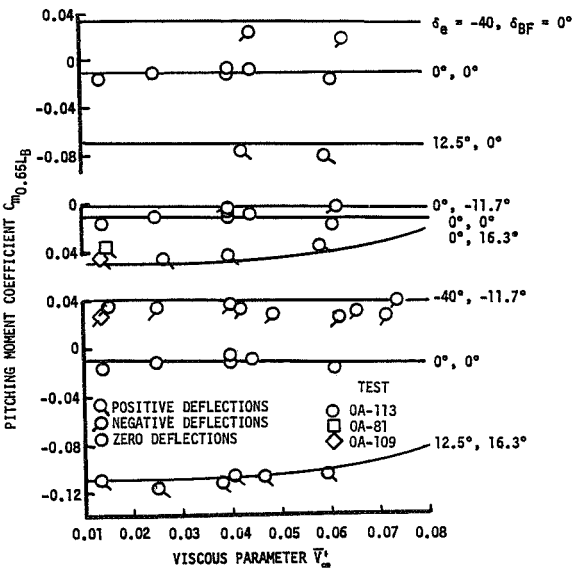

Fig. 28 EFFECTS OF VISCOUS INTERACTION PITCHING MOMENT

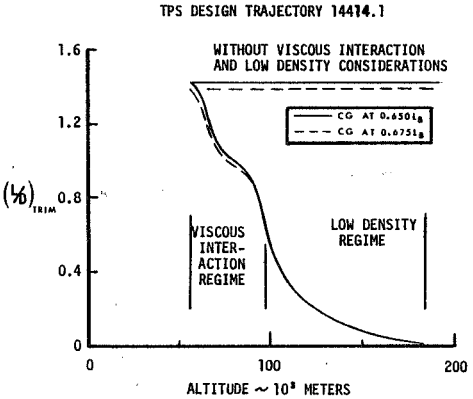

Fig. 29 VISCOUS INTERACTION EFFECT ON LIFT-TO-DRAG RATIO

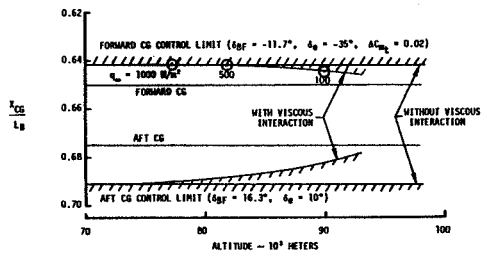

Fig. 30 VISCOUS INTERACTION EFFECT ON CG TRIM CAPABILITY

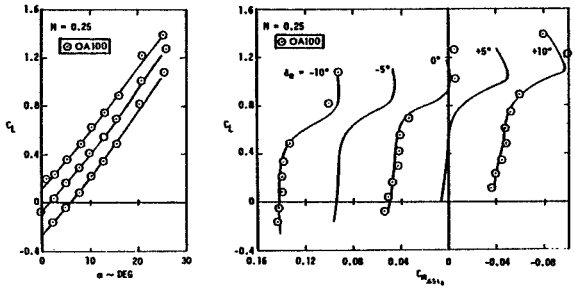

Fig. 32 LOW-SPEED LONGITUDINAL CHARACTERISTICS

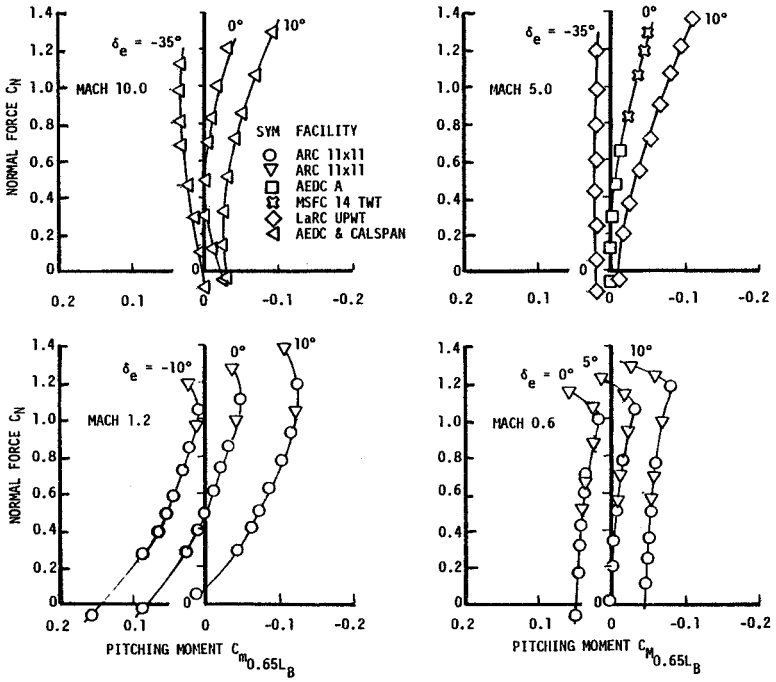

Fig. 31 LONGITUDINAL CHARACTERISTICS SUMMARY

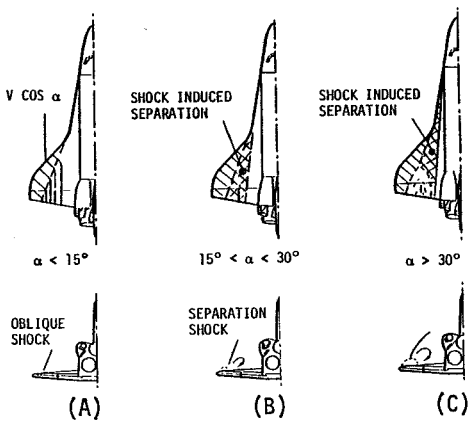

Fig. 33 LEESIDE FLOW PATTERNS

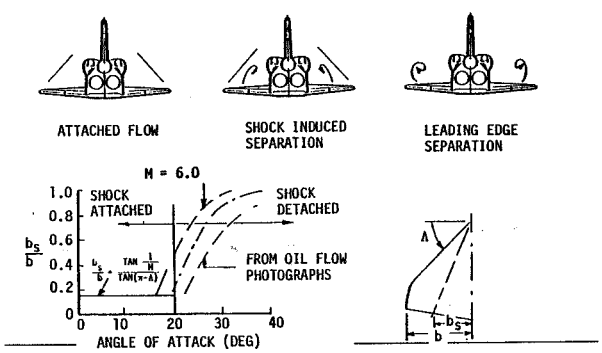

Fig. 34 LEESIDE FLOW BOUNDARIES

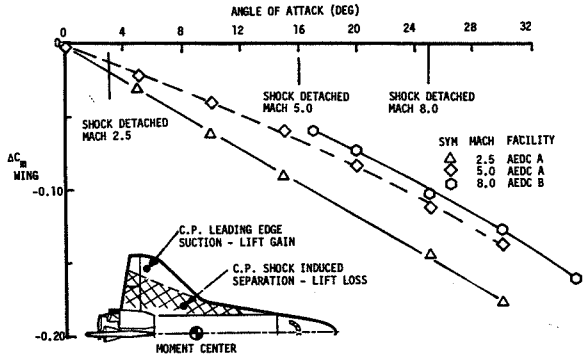

Fig. 35 LEESIDE FLOW SEPARATION EFFECT ON PITCH STABILITY

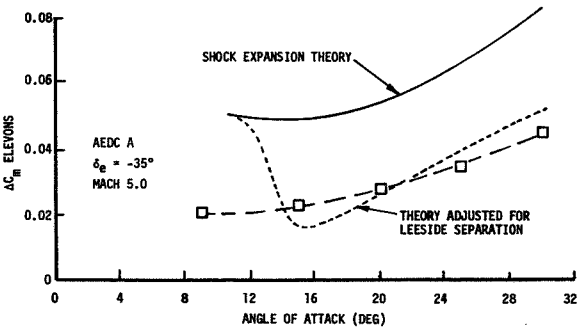

Fig. 36 HYPERSONIC CONTROL EFFECTIVENESS

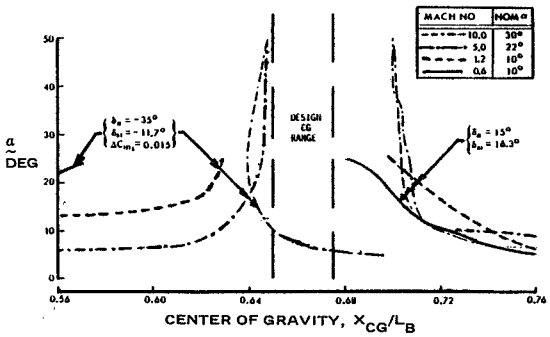

Fig. 37 TRIM CAPABILITY

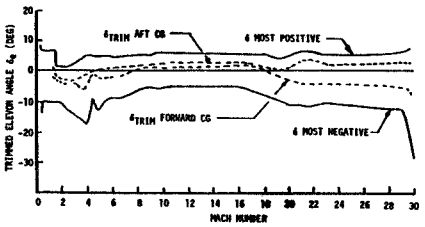

Fig. 38 ELEVON DEFLECTION SCHEDULE

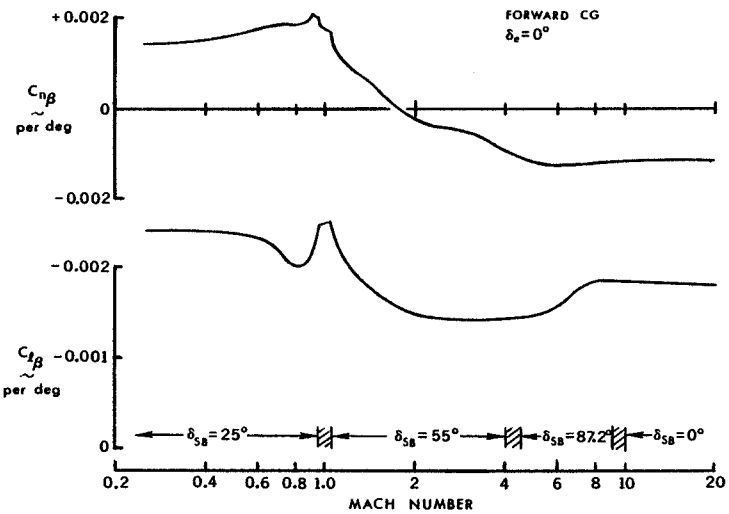

Fig. 39 LATERAL-DIRECTIONAL STABILITY DERIVATIVES

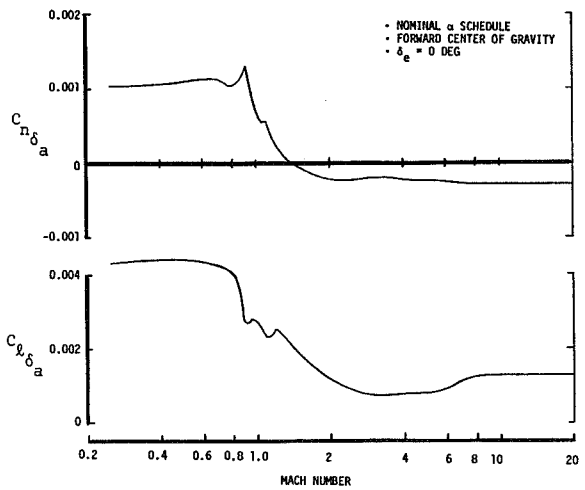

Fig. 40 AILERON EFFECTIVENESS

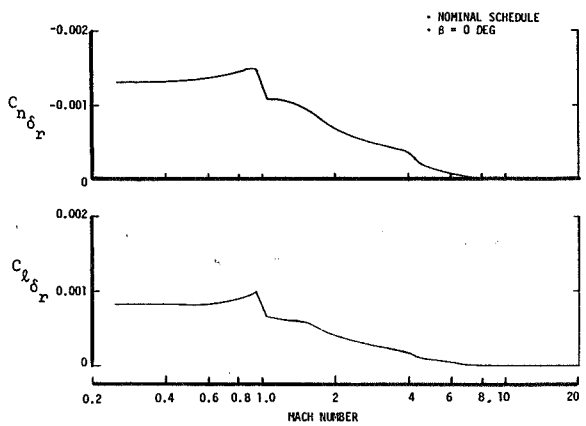

Fig. 41 RUDDER EFFECTIVENESS

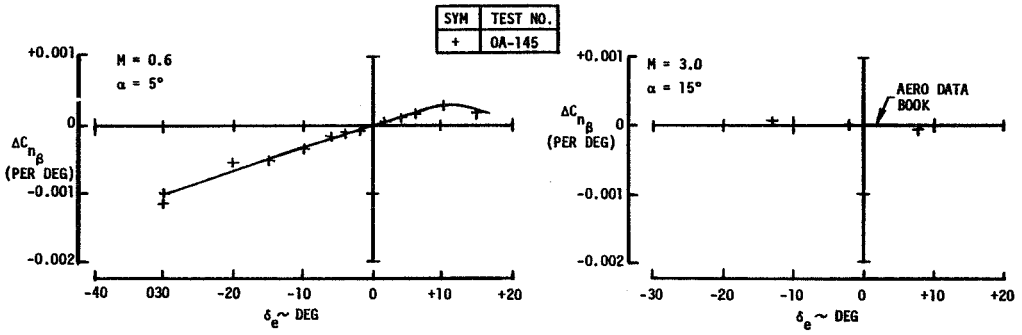

Fig. 42 EFFECT OF ELEVON DEFLECTION ON DIRECTIONAL STABILITY

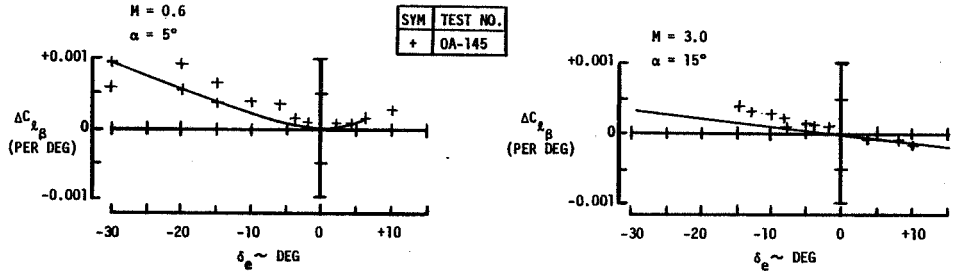

Fig. 43 EFFECT OF ELEVON DEFLECTION ON ROLL DUE TO SIDESLIP

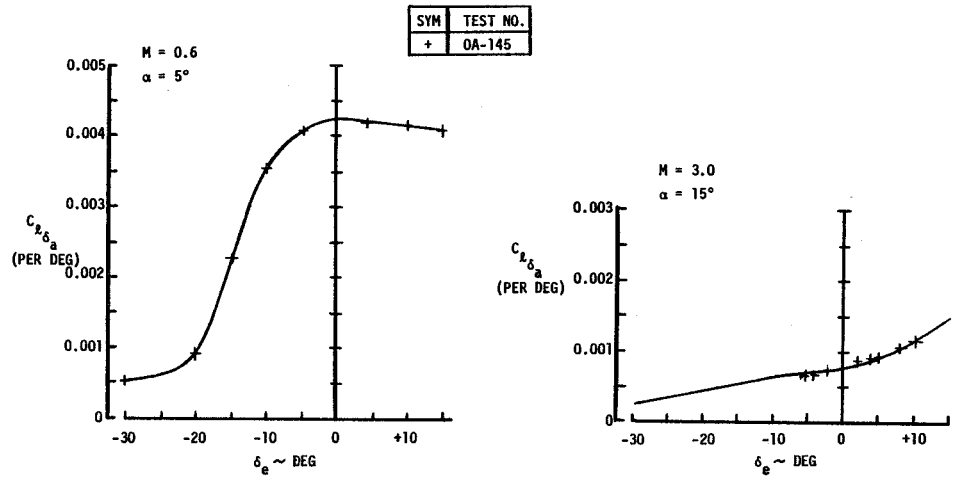

Fig. 44 EFFECT OF ELEVON DEFLECTION ON AILERON ROLL DERIVATIVE

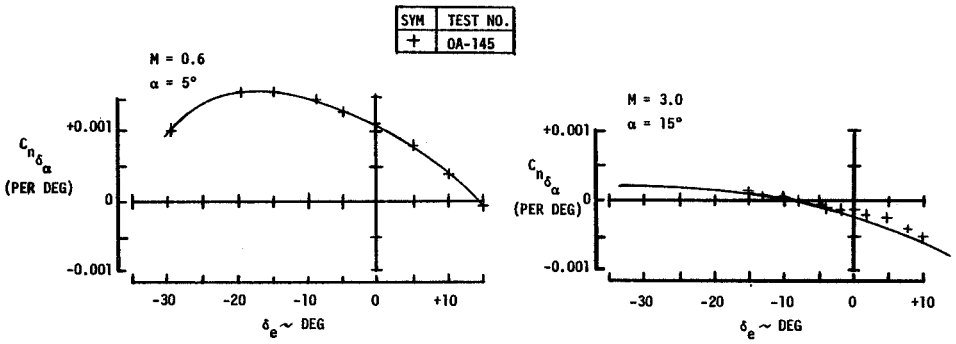

Fig. 45 EFFECT OF ELEVON DEFLECTION ON AILERON YAW DERIVATIVE

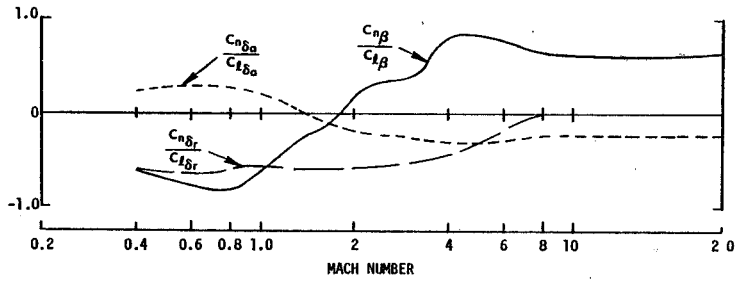

Fig. 46 CROSS COUPLING RATIOS

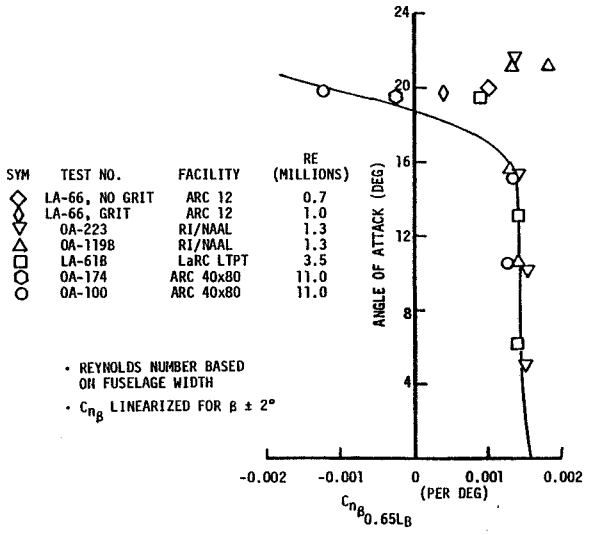

Fig. 47 EFFECT OF REYNOLDS NUMBER ON LOW-SPEED DIRECTIONAL STABILITY

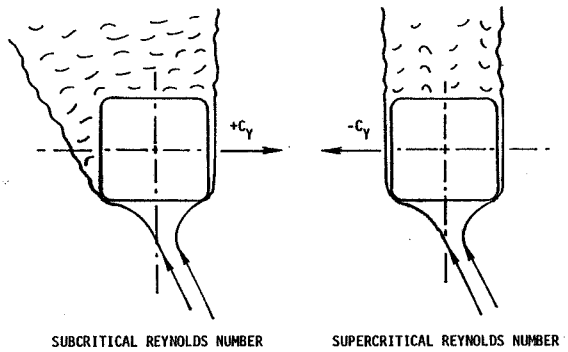

Fig. 48 ILLUSTRATION OF CROSS FLOW ON A SQUARE SHAPED CYLINDER

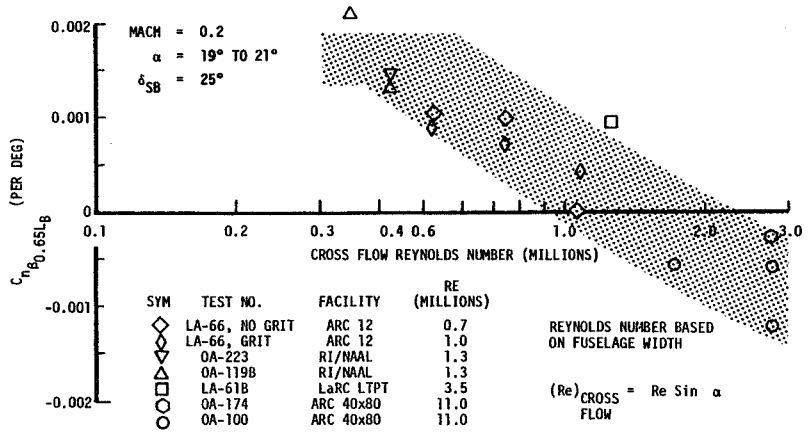

Fig. 49 VARIATION OF ORBITER DIRECTIONAL STABILITY AT HIGH ANGLE OF ATTACK WITH REYNOLDS NUMBER

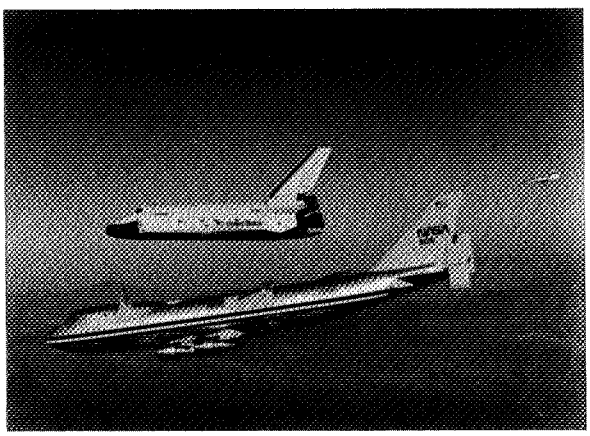

Fig. 50 ORBITER/747 SEPARATION

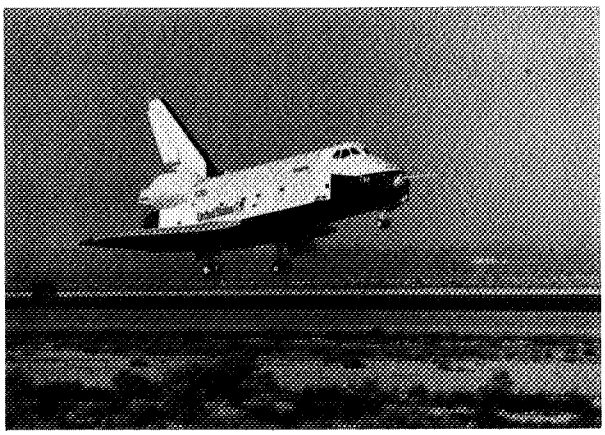

Fig. 51 ORBITER 101 LANDING

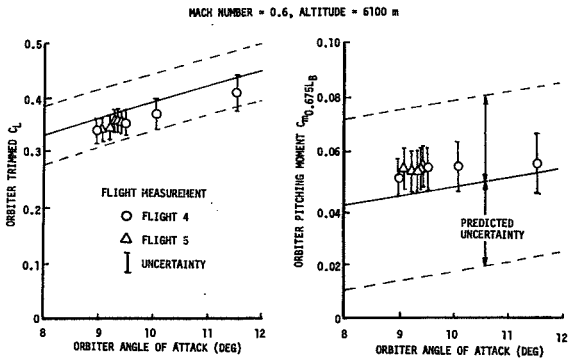

Fig. 52 COMPARISON OF FLIGHT VS. PREDICTED DATA FOR ORBITER MATED TO 747 CARRIER

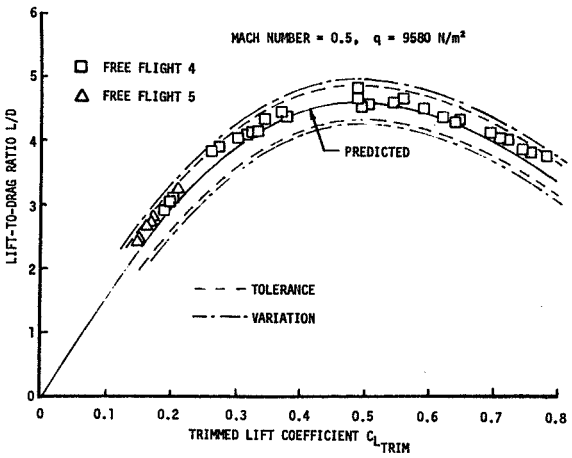

Fig. 53 COMPARISON OF FLIGHT VS. PREDICTED L/D

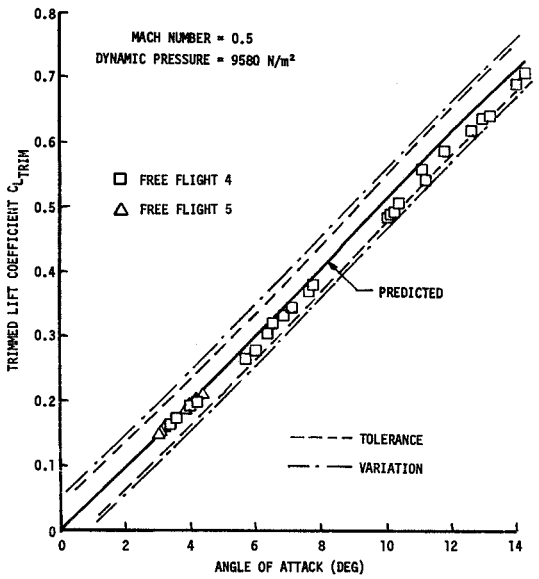

Fig. 54 COMPARISON OF FLIGHT VS. PREDICTED LIFT COEFFICIENT

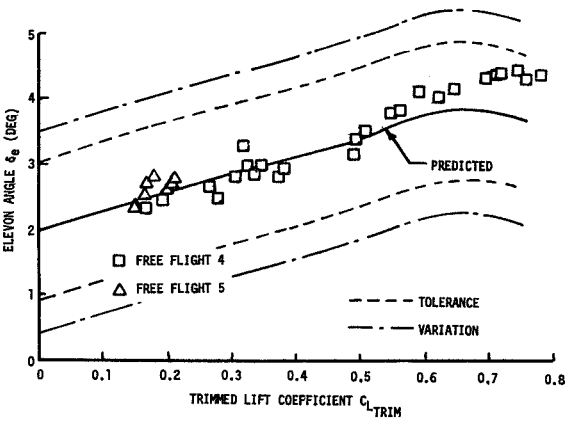

Fig. 55 COMPARISON OF FLIGHT VS. PREDICTED TRIMMED ELEVON DEFLECTION

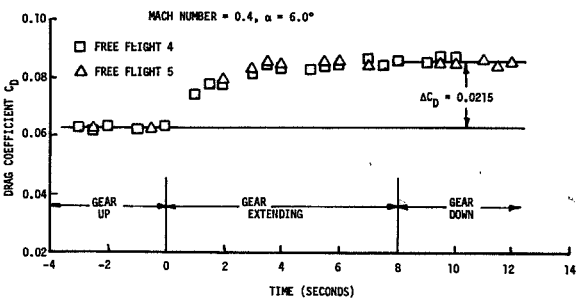

Fig. 56 COMPARISON OF FLIGHT VS. PREDICTED DRAG